Approximate Discrete-Time Small-Signal Models of DC–DC Converters With Consideration of Practical Pulsewidth Modulation and Stability Improvement Methods

Xin Li, Xinbo Ruan, *Fellow, IEEE*, Xiaoling Xiong, Mengke Sha, and Chi K Tse, *Fellow, IEEE*

***Abstract*—It is generally known that averaged models are inadequate in describing the effects of leading-edge and trailing-edge pulsewidth modulation (PWM) on the stability of dc–dc converters. In this paper, using discrete-time models of the buck, boost, and buck–boost converters and considering the effects of leading-edge and trailing-edge PWM, the general expressions of the duty-cycle-to-output-voltage transfer function, $G_{\mathrm{vd}}(z)$, in the discrete-time domain are derived. Based on the low-pass characteristics of the dc-dc converters and related properties of the matrix functions, approximate expressions of G_{vd} in the frequency domain are derived, which are simple and accurate up to half the switching frequency. Using the approximate G_{vd}, the stability of the three basic dc–dc converters under leading-edge and trailing-edge PWM is analyzed. It is shown that the stability of the buck converter is unaffected by the type of PWM, while the leading-edge modulated boost and buck–boost converters have better stability than the trailing-edge modulated ones. Since the trailing-edge modulation is commonly available in PWM controller integrated circuits, the modulation signal zero-order holding (ZOH) method and the inductor current feedback control method are proposed for use in the trailing-edge modulated boost and buck–boost converters to achieve the same effect of leading-edge modulated converters. Experimental buck and boost converters were constructed for verification of the accuracy of the proposed model and the validity of the proposed control schemes.**

***Index Terms*—Discrete-time model, leading-edge modulation, pulsewidth modulation (PWM), stability, trailing-edge modulation, zero-order hold.**

Manuscript received February 13, 2018; revised April 27, 2018 and July 12, 2018; accepted July 31, 2018. Date of publication August 9, 2018; date of current version March 29, 2019. This work was supported by the National Natural Science Foundation for Distinguished Young Scholars under Award 51525701. Recommended for publication by Associate Editor S. Kapat. *(Corresponding author: Xinbo Ruan.)*

X. Li, X. Ruan, and M. Sha are with the Center for More-Electric-Aircraft Power System, College of Automation Engineering, Nanjing University of Aeronautics and Astronautics, Nanjing 211106, China (e-mail:

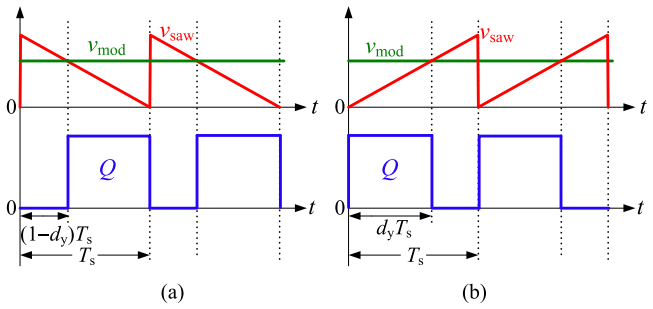

Fig. 1. Illustration of pulsewidth modulation showing triangular carrier and modulation signal (upper), and resulting pulsewidth modulated signal (lower). (a) Leading-edge modulation. (b) Trailing-edge modulation.

period has been established [14], [15]. This model is suitable for digitally controlled converters, where the sampling instant rather than the type of modulation plays a critical role in determining the converter performance. To be specific, regardless of the modulation being leading-edge or trailing-edge, off-time sampling can result in minimum-phase responses for boost or buck–boost converters. In analog controlled systems, however, the duty cycle is determined by the instantaneous value of the modulation signal at the intersecting instant. Therefore, the sampling instant is fixed at the intersecting instant, consistent with a natural sampling system [16]. The intersecting instants are different for different modulations. For the leading-edge modulation, the intersecting instant is the turn-ON instant, while for the trailing-edge modulation, the sampling instant is the turn-OFF instant. This is the primary difference between the leading-edge and trailing-edge modulations in analog controlled converters. In [7], an accurate discrete-time model of an analog controlled dc–dc converter was derived with the intersecting instant being the sampling instant, which is essentially a special case of the generalized discrete-time model [14], [15] with the ADC sampling instant set at the intersecting instant.

Accurate discrete-time models contain complex matrix exponentials, which do not offer physical insights, let alone facilitating the design process. For this purpose, a first-order approximation of the matrix exponentials (e.g., $e^{\mathbf{A}t} \approx \mathbf{I} + \mathbf{A}t$, where $\mathbf{I}$ is the unit matrix) has been applied to obtain an approximate discrete-time model based on the assumption that the state trajectories are linear [14], [15]. Furthermore, the inductor current and the output capacitor voltage have been assumed to vary approximately linearly and quadratically with time, respectively [17], [18]. This method is essentially a first-order approximation, avoiding complex matrix exponentials from the very beginning of the modeling process, and greatly simplifying the resulting model. It has been pointed out that the first-order approximation of the matrix exponentials might fail to predict the stability of dc–dc converters in some cases [19]. To solve this problem, a new bilinear approximation of the matrix exponentials has been proposed to improve the model accuracy at the expense of increased complexity [19]. The approximate discrete-time models mentioned above are all in the z-domain, which are suitable for direct loop design of digitally controlled converters. For analog controlled converters, however, an approximate model in the frequency domain is expected. There are a few standard methods transforming systems between the discrete-time domain and the frequency domain, such as zero-order hold, first-order hold, forward Euler, backward Euler, Tustin method, and Tustin method with prewarping [20]–[22]. Nevertheless, the results by these methods usually deviate from the correct result before reaching the Nyquist frequency. In [23] and [24], the average model and the discrete-time model are combined to generate an approximate frequency domain model, called discrete-time averaged model. In this combined approach, averaging has been applied to the state variables, and the discrete-time technique is applied on the output voltage. The discrete-average model has been shown to be able to distinguish different PWM schemes. This model reveals that the boost and buck–boost converters operating under the leading-edge modulation are more stable when the output capacitor has a relatively large equivalent series resistance (ESR) [25]. However, the accuracy is limited to far below the switching frequency due to the application of averaging on the state variables. As a consequence, the discrete-average model would lead to errors in stability judgment when the bandwidth is large [26]. Padé approximants have been applied to approximate the discrete-time model from the discrete-time domain to the frequency domain [26]. The result can be accurate up to the Nyquist frequency. However, the approximation of the matrix exponentials and the approximation from the discrete-time domain to the frequency domain are done separately, which is computationally demanding and must be applied for a specific converter topology. Clearly, a unified discrete-time model that is applicable to all dc–dc converters and capable of describing the effects of different PWM schemes would be very desirable.

As mentioned above, the boost and buck–boost converters operating under the leading-edge modulation are more stable [25]. However, the trailing-edge modulation is more commonly implemented in most commercially available PWM controllers. It is therefore highly desirable if a simple method can be applied to the existing PWM controllers to mimic the same characteristics of leading-edge modulated boost and buck–boost converters. Based on the above considerations, a zero-order holding (ZOH) method is incorporated in the trailing-edge modulated buck and buck–boost converters, the aim being to achieve the characteristics of the leading-edge modulated converters. In addition, in order to ensure that the leading-edge modulated converters or the trailing-edge modulated converters with modulation signal ZOH method has a large phase margin, ESR of the output filter capacitor should be increased, causing an increase in power loss and efficiency degradation [26]. To solve this problem, an inductor current feedback method is incorporated in the trailing-edge modulated buck and buck–boost converters in order to harvest the advantages of the leading-edge modulation. This method involves no change in the ESR. Thus, a capacitor with small ESR can be used, avoiding an efficiency penalty.

This paper is organized as follows. In Section II, a unified discrete-time model with sampling instant fixed at the intersection instant is derived. This model captures the effect of PWM on the stability of dc–dc converters. Section III describes the application of a general approximation method to the discrete-time

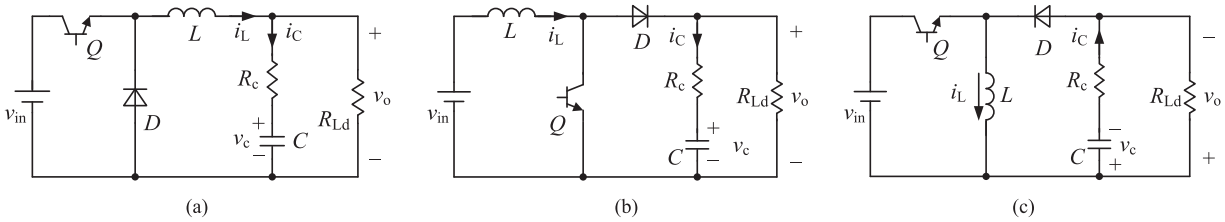

Fig. 2. Three basic dc–dc converters. (a) Buck converter. (b) Boost converter. (c) Buck–boost converter.

TABLE I
COEFFICIENT MATRICES IN STATE-SPACE EXPRESSIONS

Converters	$\mathbf{A}_1$	$\mathbf{A}_2$	$\mathbf{B}_1$	$\mathbf{B}_2$	$\mathbf{C}_1$	$\mathbf{C}_2$
Buck	$k\begin{bmatrix} -\frac{R_c}{L} & -\frac{1}{\sqrt{LC}} \\ \frac{1}{\sqrt{LC}} & -\frac{1}{R_{Ld}C} \end{bmatrix}$	$k\begin{bmatrix} -\frac{R_c}{L} & -\frac{1}{\sqrt{LC}} \\ \frac{1}{\sqrt{LC}} & -\frac{1}{R_{Ld}C} \end{bmatrix}$	$\begin{bmatrix} \frac{1}{\sqrt{L}} \\ 0 \end{bmatrix}$	$\begin{bmatrix} 0 \\ 0 \end{bmatrix}$	$k\begin{bmatrix} \frac{R_c}{\sqrt{L}} & \frac{1}{\sqrt{C}} \end{bmatrix}$	$k\begin{bmatrix} \frac{R_c}{\sqrt{L}} & \frac{1}{\sqrt{C}} \end{bmatrix}$
Boost	$k\begin{bmatrix} 0 & 0 \\ 0 & -\frac{1}{R_{Ld}C} \end{bmatrix}$	$k\begin{bmatrix} -\frac{R_c}{L} & -\frac{1}{\sqrt{LC}} \\ \frac{1}{\sqrt{LC}} & -\frac{1}{R_{Ld}C} \end{bmatrix}$	$\begin{bmatrix} \frac{1}{\sqrt{L}} \\ 0 \end{bmatrix}$	$\begin{bmatrix} \frac{1}{\sqrt{L}} \\ 0 \end{bmatrix}$	$k\begin{bmatrix} 0 & \frac{1}{\sqrt{C}} \end{bmatrix}$	$k\begin{bmatrix} \frac{R_c}{\sqrt{L}} & \frac{1}{\sqrt{C}} \end{bmatrix}$
Buck-boost	$k\begin{bmatrix} 0 & 0 \\ 0 & -\frac{1}{R_{Ld}C} \end{bmatrix}$	$k\begin{bmatrix} -\frac{R_c}{L} & -\frac{1}{\sqrt{LC}} \\ \frac{1}{\sqrt{LC}} & -\frac{1}{R_{Ld}C} \end{bmatrix}$	$\begin{bmatrix} \frac{1}{\sqrt{L}} \\ 0 \end{bmatrix}$	$\begin{bmatrix} 0 \\ 0 \end{bmatrix}$	$k\begin{bmatrix} 0 & \frac{1}{\sqrt{C}} \end{bmatrix}$	$k\begin{bmatrix} \frac{R_c}{\sqrt{L}} & \frac{1}{\sqrt{C}} \end{bmatrix}$

model, resulting in an approximate discrete-time model which adequately describes the effects of different PWM schemes on the dc–dc converters. Section IV introduces two control methods, i.e., the modulation signal ZOH method and the inductor current feedback method which are applied to trailing-edge modulated boost and buck–boost converters to achieve the same stability of the leading-edge modulated ones. To verify the accuracy of the proposed model and the effectiveness of the modulation signal ZOH method and the inductor current feedback method, experimental results are presented for the buck, boost converters in Section V. Finally, Section VI concludes this paper.

II. UNIFIED DISCRETE-TIME MODEL WITH SAMPLING TIME FIXED AT THE INTERSECTION INSTANT

The buck, boost, and buck–boost converters are shown in Fig. 2, where Q is an active switch, D is a diode, L is the inductor, C is the output filter capacitor, R_c is the ESR of C, $R_{\rm Ld}$ is the load resistor, $v_{\rm in}$ and $v_{\rm o}$ are the input and output voltages, respectively, i_L is the inductor current, and v_c is the capacitor voltage.

According to Fig. 2, the state-space descriptions of the dc–dc converters are obtained as follows [6]:

$$\frac{d\mathbf{x}(t)}{dt} = \mathbf{A}_j\mathbf{x}(t) + \mathbf{B}_j v_{\rm in}(t) \tag{1a}$$

$$v_o(t) = \mathbf{C}_j\mathbf{x}(t) \tag{1b}$$

where $j = 1$ for the on-time interval and $j = 2$ for the off-time interval. The state variable $\mathbf{x}(t)$ is defined as $[\sqrt{L}i_L(t), \sqrt{C}v_c(t)]^T$. Expressions of the coefficient matrices in the state-space equations are listed in Table I, where $k = R_{\rm Ld}/(R_c + R_{\rm Ld})$. As seen in Table I, for the buck converter, $\mathbf{C}_1 = \mathbf{C}_2$, indicating that the output voltage is continuous, whereas for the boost and buck–boost converters, $\mathbf{C}_1 \neq \mathbf{C}_2$, indicating that the output voltage is discontinuous.

By stacking the solutions of the linear equations in (1) for all subintervals over one switching period, a difference equation expressing values of the state variables at $t = (n+1)T_s + t_0$ in terms of those at $t = nT_s + t_0$, where t_0 is the time from the start of the period to the sampling instant, can be obtained as follows:

$$\begin{cases} \mathbf{x}\left[(n+1)T_s + t_0\right] = e^{\mathbf{A}_2 t_0} e^{\mathbf{A}_1 (T_s - t_0)} \mathbf{x}\left(nT_s + t_0\right) \\ \qquad + e^{\mathbf{A}_2 t_0} \displaystyle\int_0^{T_s - t_0} e^{\mathbf{A}_1 \tau} \mathbf{B}_1 v_{\rm in} d\tau + \int_0^{t_0} e^{\mathbf{A}_2 \tau} \mathbf{B}_2 v_{\rm in} d\tau \\ v_{\rm o\_dis}\left(nT_s + t_0\right) = \mathbf{C}_2 \mathbf{x}\left(nT_s + t_0\right) \end{cases} \tag{2a}$$

$$\begin{cases} \mathbf{x}\left[(n+1)T_s + t_0\right] = e^{\mathbf{A}_1 t_0} e^{\mathbf{A}_2 (T_s - t_0)} \mathbf{x}\left(nT_s + t_0\right) \\ \qquad + e^{\mathbf{A}_1 t_0} \displaystyle\int_0^{T_s - t_0} e^{\mathbf{A}_2 \tau} \mathbf{B}_2 v_{\rm in} d\tau + \int_0^{t_0} e^{\mathbf{A}_1 \tau} \mathbf{B}_1 v_{\rm in} d\tau \\ v_{\rm o\_dis}\left(nT_s + t_0\right) = \mathbf{C}_1 \mathbf{x}\left(nT_s + t_0\right). \end{cases} \tag{2b}$$

In this model, the sampling time t_0 is the instant when the modulation signal intersects with the carrier. For the leading-edge modulation, $t_0 = (1 - d_{\rm yn})T_s$, whereas for the trailing-edge modulation, $t_0 = d_{\rm yn}T_s$, where $d_{\rm yn}$ is the duty-

TABLE II
MATRICES IN DISCRETE-TIME MODEL

Matrices	Modulations	Generic expressions
$\mathbf{\Phi}$	Leading-edge	$e^{\mathbf{A}_2(1-D_y)T_s}e^{\mathbf{A}_1 D_y T_s}$
	Trailing-edge	$e^{\mathbf{A}_1 D_y T_s}e^{\mathbf{A}_2(1-D_y)T_s}$
$\mathbf{\Gamma_d}$	Leading-edge	$[(\mathbf{A}_1-\mathbf{A}_2)\mathbf{X}[(1-D_y)T_s]+(\mathbf{B}_1-\mathbf{B}_2)V_{in}]T_s$
	Trailing-edge	$[(\mathbf{A}_1-\mathbf{A}_2)\mathbf{X}(D_y T_s)+(\mathbf{B}_1-\mathbf{B}_2)V_{in}]T_s$

cycle of the nth switching period and T_s represents the switching period. So, the sampled output voltage of the leading-edge and trailing-edge modulated converter at t_0 is $\mathbf{C}_2\mathbf{x}[nT_s + (1-d_{yn})T_s]$ and $\mathbf{C}_1\mathbf{x}(nT_s + d_{yn}T_s)$, respectively.

Applying small-signal perturbation to (2), eliminating the quiescent values, and ignoring the high order ac terms, the duty-cycle-to-output-voltage transfer function of the discrete-time model in z-domain, $G_{\text{vd\_dis}}(z)$, can be expressed as follows:

$$G_{\text{vd\_dis}}(z) = \mathbf{C}_{\text{mod}}(z\mathbf{I}-\mathbf{\Phi})^{-1}\mathbf{\Phi}\mathbf{\Gamma_d} \tag{3}$$

where $\mathbf{I}$ is the unit matrix, and $\mathbf{\Phi}$ and $\mathbf{\Gamma_d}$ are the matrices in the discrete-time model, as shown in Table II. For the leading-edge modulation, $\mathbf{C}_{\text{mod}} = \mathbf{C}_2$, whereas for the trailing-edge modulation, $\mathbf{C}_{\text{mod}} = \mathbf{C}_1$.

III. APPROXIMATE DISCRETE-TIME MODEL OF DC–DC CONVERTERS

Obviously, the result in (3) is too complex to provide practical and intuitive information about the effect of the circuit parameters on stability, let alone a convenient guideline for the control loop design. In this section, a general approximation method applicable to the discrete-time model is proposed based on the low-pass characteristics of the dc–dc converters. The z-domain variables and the s-domain variables have the following relationship [27]:

$$z = e^{sT_s}. \tag{4}$$

Thus, according to Table II, $(z\mathbf{I}-\mathbf{\Phi})^{-1}\mathbf{\Phi}$ can be further expressed as follows:

$$\begin{aligned}(z\mathbf{I}-\mathbf{\Phi})^{-1}\mathbf{\Phi} &= \left[\mathbf{\Phi}^{-1}(z\mathbf{I}-\mathbf{\Phi})\right]^{-1}\\ &= \left[\left(e^{\mathbf{A}_1 D_y T_s}e^{\mathbf{A}_2(1-D_y)T_s}\right)^{-1}\left(\mathbf{I}e^{sT_s} - e^{\mathbf{A}_1 D_y T_s}e^{\mathbf{A}_2(1-D_y)T_s}\right)\right]^{-1}\end{aligned} \tag{5a}$$

for the trailing-edge modulation, and

$$\begin{aligned}(z\mathbf{I}-\mathbf{\Phi})^{-1}\mathbf{\Phi} &= \left[\mathbf{\Phi}^{-1}(z\mathbf{I}-\mathbf{\Phi})\right]^{-1}\\ &= \left[\left(e^{A_2(1-D_y)T_s}e^{\mathbf{A}_1 D_y T_s}\right)^{-1}\left(\mathbf{I}e^{sT_s} - e^{\mathbf{A}_2(1-D_y)T_s}e^{\mathbf{A}_1 D_y T_s}\right)\right]^{-1}\end{aligned} \tag{5b}$$

for the leading-edge modulation. According to [7], we have

$$e^{\mathbf{A_1}D_y T_s}e^{\mathbf{A_2}(1-D_y)T_s} \approx e^{[\mathbf{A_1}D_y + \mathbf{A_2}(1-D_y)]T_s} \tag{6a}$$

$$e^{\mathbf{A_2}(1-D_y)T_s}e^{\mathbf{A_1}D_y T_s} \approx e^{[\mathbf{A_2}(1-D_y) + \mathbf{A_1}D_y]T_s}. \tag{6b}$$

Substituting (6) into (5) yields the following:

$$\begin{aligned}&(z\mathbf{I}-\mathbf{\Phi})^{-1}\mathbf{\Phi}\\ &\approx \left[\left(e^{[\mathbf{A}_1 D_y + \mathbf{A}_2(1-D_y)]T_s}\right)^{-1}\left(\mathbf{I}e^{sT_s} - e^{[\mathbf{A}_1 D_y + \mathbf{A}_2(1-D_y)]T_s}\right)\right]^{-1}\\ &= \left[e^{[s\mathbf{I}-\mathbf{A}_1 D_y - \mathbf{A}_2(1-D_y)]T_s} - \mathbf{I}\right]^{-1}.\end{aligned} \tag{7}$$

Using the second-order Padé approximants, we obtain the approximate expression of the matrix exponential function in (7), as shown in (8) at the bottom of this page, (see Appendix A for proof).

Substituting (8) into (7) yields (9) shown at the bottom of this page. Putting (9) into (3), $G_{\text{vd\_dis}}(s)$ can be rewritten

$$\begin{aligned}e^{[s\mathbf{I}-\mathbf{A}_1 D_y - \mathbf{A}_2(1-D_y)]T_s} \approx &\left\{\mathbf{I} + 0.5\left[s\mathbf{I}-\mathbf{A}_1 D_y - \mathbf{A}_2(1-D_y)\right]T_s + \frac{\left[s\mathbf{I}-\mathbf{A}_1 D_y - \mathbf{A}_2(1-D_y)\right]^2 T_s^2}{\pi^2}\right\}\cdot\\ &\left\{\mathbf{I} - 0.5\left[s\mathbf{I}-\mathbf{A}_1 D_y - \mathbf{A}_2(1-D_y)\right]T_s + \frac{\left[s\mathbf{I}-\mathbf{A}_1 D_y - \mathbf{A}_2(1-D_y)\right]^2 T_s^2}{\pi^2}\right\}^{-1}\end{aligned} \tag{8}$$

$$\begin{aligned}(z\mathbf{I}-\mathbf{\Phi})^{-1}\mathbf{\Phi} &\approx \left\{\begin{bmatrix}\mathbf{I} + 0.5\left(s\mathbf{I}-\mathbf{A}_1 D_y - \mathbf{A}_2(1-D_y)\right)T_s + \frac{(s\mathbf{I}-\mathbf{A}_1 D_y - \mathbf{A}_2(1-D_y))^2 T_s^2}{\pi^2}\end{bmatrix}\cdot\right.\\ &\left.\begin{bmatrix}\mathbf{I} - 0.5\left(s\mathbf{I}-\mathbf{A}_1 D_y - \mathbf{A}_2(1-D_y)\right)T_s + \frac{(s\mathbf{I}-\mathbf{A}_1 D_y - \mathbf{A}_2(1-D_y))^2 T_s^2}{\pi^2}\end{bmatrix}^{-1} - \mathbf{I}\right\}^{-1}\\ &= \left\{\begin{Bmatrix}\mathbf{I} + 0.5\left(s\mathbf{I}-\mathbf{A}_1 D_y - \mathbf{A}_2(1-D_y)\right)T_s + \frac{(s\mathbf{I}-\mathbf{A}_1 D_y - \mathbf{A}_2(1-D_y))^2 T_s^2}{\pi^2}\\ -\mathbf{I} + 0.5\left(s\mathbf{I}-\mathbf{A}_1 D_y - \mathbf{A}_2(1-D_y)\right)T_s - \frac{(s\mathbf{I}-\mathbf{A}_1 D_y - \mathbf{A}_2(1-D_y))^2 T_s^2}{\pi^2}\end{Bmatrix}\cdot\right.\\ &\left.\left\{\mathbf{I} - 0.5\left(s\mathbf{I}-\mathbf{A}_1 D_y - \mathbf{A}_2(1-D_y)\right)T_s + \frac{(s\mathbf{I}-\mathbf{A}_1 D_y - \mathbf{A}_2(1-D_y))^2 T_s^2}{\pi^2}\right\}^{-1}\right\}^{-1}\\ &= \left\{\left(s\mathbf{I}-\mathbf{A}_1 D_y - \mathbf{A}_2(1-D_y)\right)T_s\left[\mathbf{I} - 0.5\left(s\mathbf{I}-\mathbf{A}_1 D_y - \mathbf{A}_2(1-D_y)\right)T_s + \frac{\left(s\mathbf{I}-\mathbf{A}_1 D_y - \mathbf{A}_2(1-D_y)\right)^2 T_s^2}{\pi^2}\right]^{-1}\right\}^{-1}\\ &= \left[\left(s\mathbf{I}-\mathbf{A}_1 D_y - \mathbf{A}_2(1-D_y)\right)T_s\right]^{-1} - 0.5\mathbf{I} + \frac{\left(s\mathbf{I}-\mathbf{A}_1 D_y - \mathbf{A}_2(1-D_y)\right)T_s}{\pi^2}\end{aligned} \tag{9}$$

as follows:

$$G_{\mathrm{vd\_dis}}(s) = \mathbf{C}_{\mathrm{mod}}\left[(s\mathbf{I} - \mathbf{A_1}D_y - \mathbf{A_2}(1-D_y))\,T_s\right]^{-1}\mathbf{\Gamma_d} - 0.5\mathbf{C}_{\mathrm{mod}}\,\mathbf{\Gamma_d} + \mathbf{C}_{\mathrm{mod}}\,\frac{(s\mathbf{I} - \mathbf{A_1}D_y - \mathbf{A_2}(1-D_y))\,T_s}{\pi^2}\mathbf{\Gamma_d}. \tag{10}$$

In the following, the expression of $\mathbf{\Gamma_d}$ will be approximated. Taking the trailing-edge modulated boost converter as an example, the approximation process of $\mathbf{\Gamma_d}$ will be given below.

The inductor current i_L arrives at its peak value at $t = D_yT_s$, and can be expressed as follows:

$$I_L\left(D_yT_s\right) = \frac{V_{\mathrm{in}}}{\left(1-D_y\right)^2 R_{\mathrm{Ld}}} + \frac{V_{\mathrm{in}}}{2L}D_yT_s. \tag{11}$$

Considering the switching ripple of the capacitor voltage being much lower than its dc value, the value of $V_c(D_yT_s)$ can be represented by its dc value, i.e.,

$$V_c\left(D_yT_s\right) = \frac{V_{\mathrm{in}}}{1-D_y}. \tag{12}$$

From (11) and (12), $\mathbf{X}(D_yT_s)$ is approximated to be

$$\mathbf{X}\left(D_yT_s\right) \approx \begin{bmatrix} \sqrt{L}\left(\frac{V_{\mathrm{in}}}{\left(1-D_y\right)^2 R_{\mathrm{Ld}}} + \frac{V_{\mathrm{in}}}{2L}D_yT_s\right) \\ \sqrt{C}\frac{V_{\mathrm{in}}}{1-D_y} \end{bmatrix}. \tag{13}$$

Moreover, from Table I and (13), an approximate expression of $\mathbf{\Gamma_d}$ can be written as follows:

$$\mathbf{\Gamma_d} = V_{\mathrm{in}}\begin{bmatrix} \frac{R_c}{\left(1-D_y\right)^2\sqrt{L}R_{\mathrm{Ld}}} + \frac{R_cD_yT_s}{2L\sqrt{L}} + \frac{1}{\left(1-D_y\right)\sqrt{L}} \\ -\left(\frac{1}{\left(1-D_y\right)^2 R_{\mathrm{Ld}}\sqrt{C}} + \frac{D_yT_s}{2L\sqrt{C}}\right) \end{bmatrix} T_s. \tag{14}$$

Substituting the expression of each coefficient matrix, the s-domain duty-cycle-to-output-voltage transfer function of the trailing-edge modulated boost converter, $G_{\mathrm{vd\_dis\_trail\_bst}}(s)$ is derived as (15) at the bottom of this page.

Normally, in order to achieve small switching ripple in the output voltage of a dc–dc converter, the following approximate conditions are assumed when choosing the circuit parameters, i.e.,

$$R_{\mathrm{Ld}}C >> T_s,\ \frac{L}{R_c} >> T_s,\ LC >> {T_s}^2. \tag{16}$$

According to (16), the coefficient of the constant term in the numerator of (15) can be approximated as follows:

$$1 + \frac{{T_s}^2}{LC}(1-D_y)^2\left(\frac{D_y}{4} - \frac{1}{\pi^2}\right) + \frac{T_s}{2R_{\mathrm{Ld}}C} \approx 1. \tag{17}$$

The coefficient of the s term in the numerator of (15) can be approximated as follows:

$$\frac{D_yT_s}{2} + \frac{L}{\left(1-D_y\right)^2 R_{\mathrm{Ld}}} + \frac{D_y\left(1-D_y\right)^2T_s^3}{2\pi^2LC} - \frac{R_cT_s}{2R_{\mathrm{Ld}}\left(1-D_y\right)} - \frac{\left(1-D_y\right)R_cT_s^2}{L}\left(\frac{D_y}{4} - \frac{1}{\pi^2}\right) + \frac{T_s^2}{R_{\mathrm{Ld}}C}\left(\frac{2}{\pi^2} - \frac{D_y}{4}\right) - \frac{LT_s}{2R_{\mathrm{Ld}}^2C\left(1-D_y\right)^2} \approx \frac{D_yT_s}{2} + \frac{L}{\left(1-D_y\right)^2R_{\mathrm{Ld}}}. \tag{18}$$

The coefficients of the s^2 term in the numerator of (15) can be approximated as follows:

$$\frac{LT_s}{2R_{\mathrm{Ld}}(1-D_y)^2} + \left(\frac{D_y}{4} - \frac{1}{\pi^2}\right)T_s^2 - \frac{R_cT_s^2}{\pi^2\left(1-D_y\right)R_{\mathrm{Ld}}} - \frac{D_y\left(1-D_y\right)R_cT_s^3}{2\pi^2L} - \frac{LT_s^2}{\pi^2(1-D_y)^2R_{\mathrm{Ld}}^2C} - \frac{D_yT_s^3}{2\pi^2R_{\mathrm{Ld}}C} \approx \frac{LT_s}{2R_{\mathrm{Ld}}(1-D_y)^2} + \left(\frac{D_y}{4} - \frac{1}{\pi^2}\right)T_s^2. \tag{19}$$

According to (17)–(19), $G_{\mathrm{vd\_dis\_trail\_bst}}(s)$ can be approximated as follows:

$$G_{\mathrm{vd\_dis\_trail\_bst}}(s) = \frac{V_{\mathrm{in}}}{LC}\frac{1 - s\left[\frac{D_yT_s}{2} + \frac{L}{\left(1-D_y\right)^2R_{\mathrm{Ld}}}\right]\left[1 - \frac{sT_s}{2} + \left(\frac{sT_s}{\pi}\right)^2\right] - \left(\frac{sT_s}{\pi}\right)^2}{s^2 + s\left[\left(1-D_y\right)\frac{R_c}{L} + \frac{1}{R_{\mathrm{Ld}}C}\right] + \frac{\left(1-D_y\right)^2}{LC}}. \tag{20}$$

Likewise, the approximate expressions of $G_{\mathrm{vd\_dis}}(s)$ for buck, boost, and buck–boost converters with trailing-edge and leading-edge modulations can be obtained, i.e.,

$$G_{\mathrm{vd\_dis\_bu}}(s) = \frac{V_{\mathrm{in}}}{LC}\frac{1 + sR_cC\left[1 - \frac{sT_s}{2} + \left(\frac{sT_s}{\pi}\right)^2\right] - \frac{T_s^2}{\pi^2R_{\mathrm{Ld}}C}s - \frac{T_s^2}{\pi^2}s^2}{s^2 + s\left(\frac{R_c}{L} + \frac{1}{R_{\mathrm{Ld}}C}\right) + \frac{1}{LC}} \tag{21}$$

$$G_{\mathrm{vd\_dis\_trail\_bst}}(s) = V_{\mathrm{in}}\frac{\begin{array}{l} 1 + \frac{T_s^2}{LC}(1-D_y)^2\left(\frac{D_y}{4} - \frac{1}{\pi^2}\right) + \frac{T_s}{2R_{\mathrm{Ld}}C} \\ -\begin{bmatrix} \frac{D_yT_s}{2} + \frac{L}{(1-D_y)^2R_{\mathrm{Ld}}} + \frac{D_y(1-D_y)^2T_s^3}{2\pi^2LC} - \frac{R_cT_s}{2R_{\mathrm{Ld}}(1-D_y)} \\ -\frac{(1-D_y)R_cT_s^2}{L}\left(\frac{D_y}{4} - \frac{1}{\pi^2}\right) + \frac{T_s^2}{R_{\mathrm{Ld}}C}\left(\frac{2}{\pi^2} - \frac{D_y}{4}\right) - \frac{LT_s}{2R_{\mathrm{Ld}}^2C(1-D_y)^2} \end{bmatrix}s \\ +\begin{bmatrix} \frac{LT_s}{2R_{\mathrm{Ld}}(1-D_y)^2} + \left(\frac{D_y}{4} - \frac{1}{\pi^2}\right)T_s^2 - \frac{R_cT_s^2}{\pi^2(1-D_y)R_{\mathrm{Ld}}} \\ -\frac{D_y(1-D_y)R_cT_s^3}{2\pi^2L} - \frac{LT_s^2}{\pi^2(1-D_y)^2R_{\mathrm{Ld}}^2C} - \frac{D_yT_s^3}{2\pi^2R_{\mathrm{Ld}}C} \end{bmatrix}s^2 - \left[\frac{LT_s^2}{\pi^2(1-D_y)^2R_{\mathrm{Ld}}} + \frac{D_yT_s^3}{2\pi^2}\right]s^3 \end{array}}{LCs^2 + \left[\left(1-D_y\right)R_cC + \frac{L}{R_{\mathrm{Ld}}}\right]s + \left(1-D_y\right)^2} \tag{15}$$

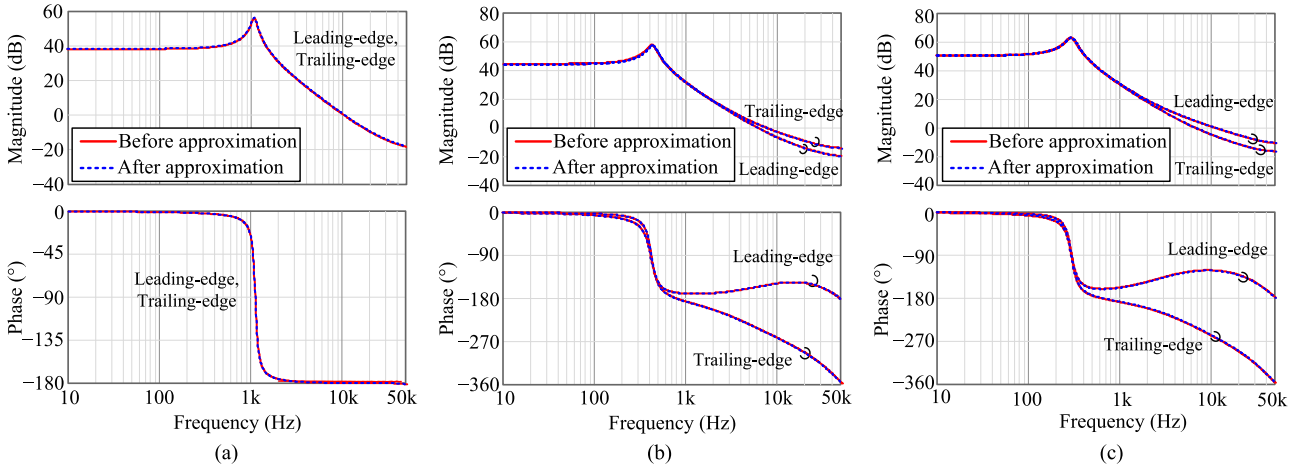

Fig. 3. Bode diagrams of $G_{\text{vd\_dis}}(s)$ before and after approximation for (a) buck converter, (b) boost converter, and (c) buck–boost converter.

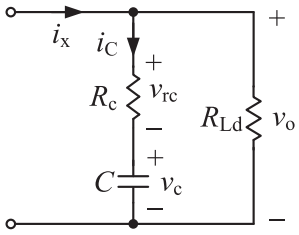

Fig. 4. Schematic diagram of the output terminals of three basic dc–dc converters.

where $m = 1$ for the leading-edge modulation, and $m = 0$ for the trailing-edge modulation. Equations (22) and (23) as shown at the bottom of this page.

To verify the validity of the approximation method, Fig. 3 gives the Bode diagrams of $G_{\text{vd\_dis}}(s)$ before and after approximation, where the detailed circuit parameters of the three basic dc–dc converters are shown in Appendix B.

As seen from Fig. 3, $G_{\text{vd\_dis}}(s)$ for the buck converter is identical under the two PWM schemes, while $G_{\text{vd\_dis\_lead}}(s)$ leads $G_{\text{vd\_dis\_trail}}(s)$ in phase for the boost and buck–boost converters. The explanation is given below. The output terminals of the buck, boost, and buck–boost converters are shown in Fig. 4, in which i_x represents the sum of the output filter capacitor current i_C and the output current. Note that i_C is the ac component of i_x.

For the buck converter, i_x is the inductor current i_L, which is continuous. Therefore, both i_C and output voltage v_o are continuous. As a result, the relationship among v_o, i_L, and v_c remains the same regardless of the PWM scheme used, which means the expressions of $G_{\text{vd\_dis}}(s)$ for the buck converter under the leading-edge and trailing-edge modulations are identical.

For the boost and buck–boost converters, however, i_x is the diode current i_D, which is discontinuous. Thus, i_C and v_o will have a step change at the turn-ON and turn-OFF instants. According to the discrete-time model, the sampled output voltage under the trailing-edge modulation is $\mathbf{C}_1\mathbf{x}(nT_s + d_{\text{yn}}T_s) = kv_c(nT_s + d_{\text{yn}}T_s)$, while the sampled output voltage under the leading-edge modulation is $\mathbf{C}_2\mathbf{x}[nT_s + (1 - d_{\text{yn}})T_s] = kv_c[nT_s + (1-d_{\text{yn}})T_s] + kR_c i_L[nT_s + (1-d_{\text{yn}})T_s]$, which contains information related to the inductor current due to the presence of the ESR. Since $i_L(t)$ leads $v_c(t)$ in phase, the output voltage under the leading-edge modulation has a leading phase angle under the same duty-cycle perturbation. In other words, for the boost and buck–boost converters, $G_{\text{vd\_dis\_lead}}(s)$ leads $G_{\text{vd\_dis\_trail}}(s)$ in phase.

In [25], the discrete-average model was successfully used in analyzing the difference between the leading-edge modulation and the trailing-edge modulation. However, the discrete-average model still adopts the concept of averaging, and is not that accurate at high frequencies. Taking the boost converter for example, Fig. 5 has a comparison between the discrete-average model and the proposed model under both leading-edge and trailing-edge modulation. As we can see, the discrete-average model tends to predict a higher phase in high-frequency range under both modulations, which would lead to errors in stability judgment when the bandwidth gets higher. Therefore, the proposed model is more suitable in wideband control applications.

$$G_{\text{vd\_dis\_bst}}(s) = \frac{V_{\text{in}}}{LC}\frac{1 + s\left[\left(m-\frac{1}{2}\right)D_yT_s + m\frac{R_cC}{1-D_y} - \frac{L}{(1-D_y)^2R_{\text{Ld}}}\right]\left[1 - \frac{sT_s}{2} + \left(\frac{sT_s}{\pi}\right)^2\right] - \left(\frac{sT_s}{\pi}\right)^2}{s^2 + s\left[(1-D_y)\frac{R_c}{L} + \frac{1}{R_{\text{Ld}}C}\right] + \frac{(1-D_y)^2}{LC}} \tag{22}$$

$$G_{\text{vd\_dis\_bb}}(s) = \frac{V_{\text{in}}}{LC}\frac{1 + s\left[\left(m-\frac{1}{2}\right)D_yT_s + m\frac{R_cC}{1-D_y} - \frac{D_yL}{(1-D_y)^2R_{\text{Ld}}}\right]\left[1 - \frac{sT_s}{2} + \left(\frac{sT_s}{\pi}\right)^2\right] - \left(\frac{sT_s}{\pi}\right)^2}{s^2 + s\left[(1-D_y)\frac{R_c}{L} + \frac{1}{R_{\text{Ld}}C}\right] + \frac{(1-D_y)^2}{LC}} \tag{23}$$

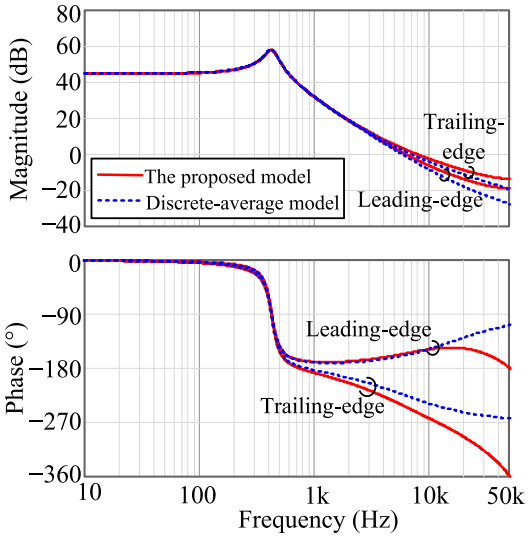

Fig. 5. Bode diagrams of $G_{\rm vd}$ from the discrete-average model and the proposed model.

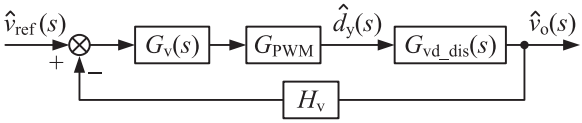

Fig. 6. Control block diagram of a dc–dc converter.

IV. Control Methods to Equivalently Achieve Trailing-Edge Modulation

A. Modulation Signal Zero-Order Holding Method

The control block diagram of a dc–dc converter is shown in Fig. 6, where H_v is the sensor gain of the output voltage. Also, $G_{\rm PWM}$ is the transfer function of the PWM modulator and its magnitude is the reciprocal of the amplitude V_m of the triangular carrier, and $G_v(s)$ is the transfer function of the voltage regulator.

As shown in Fig. 6, the loop gain, $T_{\rm dis}(s)$, can be expressed as follows:

$$T_{\rm dis}(s) = H_v G_{\rm PWM} G_v(s) G_{\rm vd\_dis}(s). \tag{24}$$

From the theoretical analysis presented above, we know that for the boost and buck–boost converters, $G_{\rm vd\_dis\_lead}(s)$ has a leading phase angle relative to $G_{\rm vd\_dis\_trail}(s)$. Thus, the leading-edge modulated boost and buck–boost converters will have better stability than the trailing-edge modulated ones when adopting the same voltage regulator. However, almost all commercially available PWM control ICs adopt the trailing-edge modulation. It is thus necessary to equivalently realize the leading-edge modulation with the trailing-edge modulation PWM controllers. For this purpose, this paper presents a modulation ZOH method first.

According to (3), the advantage of the leading-edge modulation lies in that the sampling instant is at the instant right before the switch is turned ON. Therefore, if the sampling instant of the trailing-edge modulation is moved to the instant right before the turn-on instant of the switch, then the effect of the leading-edge modulation can be realized. This can be implemented via introducing a zero-order holder at the output of the controller. After being sampled and held by the zero-order holder, the new modulation signal will become flat. The duty cycle is determined by the new modulation signal intersecting the carrier wave. This method is called *modulation signal ZOH method*. Fig. 7(a) and (b) give the control scheme diagram and key waveforms of the modulation signal ZOH method, respectively, where $v_{\rm sp}$ is the sampling pulse. For most analog PWM control ICs, the clock signal is a narrow pulse at the beginning of every switching period, the falling edge of which occurs before the turn-ON instant of the switch. Hence, the clock signal can be directly used as the sampling pulse $v_{\rm sp}$. Also, $v_{\rm mod\_ZOH}$ is the new modulation signal, which is flat as analyzed.

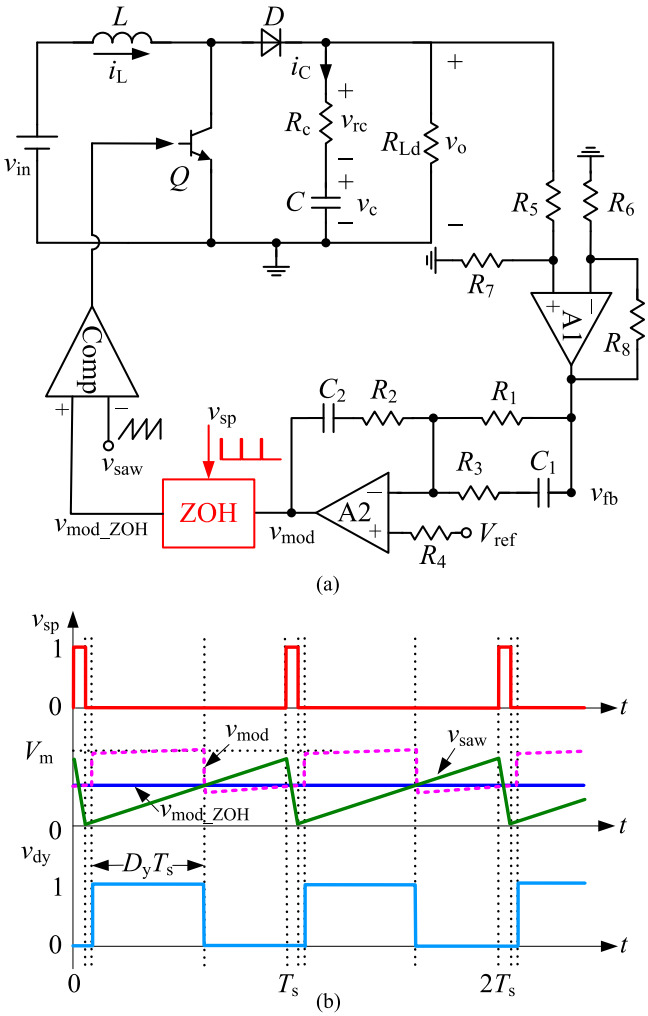

Fig. 7. Modulation signal ZOH method of the trailing-edge modulated boost converter. (a) Circuit schematic. (b) Key waveforms.

It should be noted that the modulation signal ZOH method will inevitably introduce D_yT_s delay by the sample and hold effect [13], resulting in a phase lag in the loop. Considering this, if the ESR of the output capacitor is too small to improve the phase margin, the zero-order holding method may not work in

stability improvement. One has to take it into account before using this method. In our case, it can be seen from Fig. 3(b) that in the boost converter, the leading-edge modulation leads the trailing-edge modulation by 66° at the cut-off frequency (around 4 kHz, as given in Section V), whereas the phase lag introduced by the sample and hold effect is only 8° at the cut-off frequency, therefore this method is quite useful here.

Although this method is implemented in analog form here, it can be implemented in digital control using digital control ICs that contain a built-in zero-order holder. However, digital control methods may introduce an additional computational delay. The computational delay is usually equal to the switching period, T_s, which leads to a larger phase lag of the converter. In contrast, analog control has no computational delay, thus is more stable.

B. Inductor Current Feedback Method

As mentioned previously, if the ESR of the output capacitor is too small to affect the dynamics of boost and buck–boost converters, the use of leading-edge modulation or the zero-order holding method does not contribute to stability improvement. In this case, it is necessary to increase the ESR of the output capacitor to widen the phase margin. Unfortunately, this will incur extra power loss and degrade the efficiency. Thus, it is practically desirable to derive a simple method that can make commercial PWM control chips with trailing-edge modulation achieve the same stability level as the leading-edge modulated boost and buck–boost converters without increasing the value of ESR.

According to the analysis above, the output voltage expression of the trailing-edge modulated boost and buck–boost converters is as follows:

$$v_{\text{o\_dis\_trail}} = \mathbf{C_1 x}\left(d_{\text{yn}}T_s\right) = kv_c\left(d_{\text{yn}}T_s\right). \tag{25}$$

Also, the output voltage expression of the leading-edge modulated boost and buck–boost converters is as follows:

$$\begin{aligned} v_{\text{o\_dis\_lead}} &= \mathbf{C_2 x}\left[\left(1-d_{\text{yn}}\right)T_s\right] \\ &= kv_c\left[\left(1-d_{\text{yn}}\right)T_s\right] + kR_c i_L\left[\left(1-d_{\text{yn}}\right)T_s\right]. \end{aligned} \tag{26}$$

Comparing (25) and (26), it can be found that the output voltage of the trailing-edge modulated converter misses the $kR_c i_L$ term. For this reason, we may add this term into the output voltage under the trailing-edge modulation and make it identical to the output voltage of the leading-edge modulated converters. With this consideration, the new output voltage under the trailing-edge modulation can be rewritten as follows:

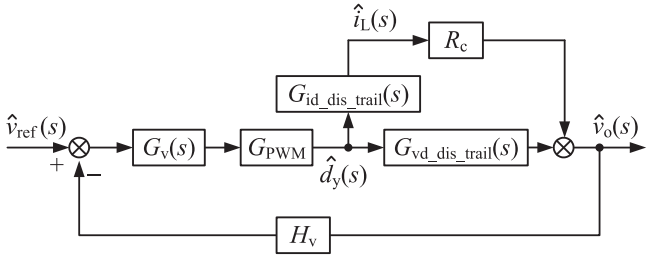

Fig. 8. Control block diagram of dc–dc converters with inductor current feedback.

$$v_{\text{o\_dis\_trail\_com}} = \mathbf{C_2 x}\left(d_{\text{yn}}T_s\right) = kv_c\left(d_{\text{yn}}T_s\right) + kR_c i_L\left(d_{\text{yn}}T_s\right). \tag{27}$$

Adding $kR_c i_L$ into the output voltage for the trailing-edge modulated converters can be realized via applying inductor current feedback, as shown in Fig. 8, where $G_{\text{id\_dis\_trail}}(s)$ represents the duty-cycle-to-inductor-current transfer function of the discrete-time model under the trailing-edge modulation, and will be derived below with the example of the boost converter.

Since the current flowing through R_c is the ac component of the inductor current, this ac component of the inductor current is fed back in the control loop. Note that since this method involves no change in the ESR of the output capacitor, the efficiency of the converters will not be affected.

Similar to the derivation of $G_{\text{vd\_dis}}$ in Section II, the duty-cycle-to-state-variable transfer function matrix can be expressed as follows:

$$G_{\mathbf{x}\text{d}}(z) = \left.\frac{\hat{\mathbf{x}}(z)}{\hat{d}_{\text{yn}}(z)}\right|_{\hat{v}_{\text{in}}=0} = \left(z\mathbf{I}-\mathbf{\Phi}\right)^{-1}\mathbf{\Phi\Gamma_d} \tag{28}$$

where $\mathbf{x}(t) = [\sqrt{L}i_L(t), \sqrt{C}v_c(t)]^T$. According to (14) and (28), the expression of $G_{\text{id\_dis\_bst\_trail}}(s)$ for the boost converter is given as (29) at the bottom of this page.

With the approximate conditions given in (16), the coefficient of the constant term in the numerator of (29) can be approximated as follows:

$$\begin{aligned} &\frac{R_c}{\left(1-D_y\right)R_{\text{Ld}}^2 C} + \frac{D_y\left(1-D_y\right)R_c T_s}{2LCR_{\text{Ld}}} + \frac{2}{R_{\text{Ld}}C} - \frac{\left(1-D_y\right)^3 T_s}{2LC} \\ &\quad\approx \frac{2}{R_{\text{Ld}}C} - \frac{\left(1-D_y\right)^3 T_s}{2LC}. \end{aligned} \tag{30}$$

$$G_{\text{id\_dis\_trail\_bst}}(s) = \frac{V_{\text{in}}}{(1-D_y)L} \frac{\begin{aligned}&\frac{R_c}{(1-D_y)R_{\text{Ld}}^2 C} + \frac{D_y(1-D_y)R_c T_s}{2LCR_{\text{Ld}}} + \frac{2}{R_{\text{Ld}}C} - \frac{(1-D_y)^3 T_s}{2LC} \\ &+\left[1 + \frac{R_c}{(1-D_y)R_{\text{Ld}}} + \frac{D_y(1-D_y)R_c T_s}{2L} \right.\\ &\left.+\frac{(1-D_y)^2 T_s^2}{\pi^2 LC} - \frac{(1-D_y)R_c T_s}{2L} - \frac{T_s}{2R_{\text{Ld}}C}\right] s + \left[\frac{(1-D_y)R_c T_s^2}{\pi^2 L} + \frac{T_s^2}{\pi^2 R_{\text{Ld}}C} - \frac{T_s}{2}\right] s^2 + \frac{T_s^2}{\pi^2} s^3\end{aligned}}{s^2 + \left[(1-D_y)\frac{R_c}{L} + \frac{1}{R_{\text{Ld}}C}\right] s + \frac{(1-D_y)^2}{LC}} \tag{29}$$

The coefficients of the s term in the numerator of (29) can be approximated as follows:

$$1+\frac{R_c}{(1-D_y)R_{\rm Ld}}+\frac{D_y(1-D_y)R_cT_s}{2L}+\frac{(1-D_y)^2T_s^2}{\pi^2LC}-\frac{(1-D_y)R_cT_s}{2L}-\frac{T_s}{2R_{\rm Ld}C}\approx 1. \tag{31}$$

The coefficients of the s^2 term in the numerator of (29) can be approximated as follows:

$$\frac{(1-D_y)R_cT_s^2}{\pi^2L}+\frac{T_s^2}{\pi^2R_{\rm Ld}C}-\frac{T_s}{2}\approx-\frac{T_s}{2} \tag{32}$$

According to (30)–(32), the expression of the duty-cycle-to-inductor-current transfer function, $G_{\rm id\_dis\_trail\_bst}(s)$, can be approximated as follows:

$$G_{\rm id\_dis\_trail\_bst}(s)=\frac{V_{\rm in}}{LC(1-D_y)}\frac{\frac{2}{R_{\rm Ld}}-\frac{(1-D_y)^3T_s}{2L}+Cs\left(1-\frac{T_s}{2}s+\frac{T_s^2}{\pi^2}s^2\right)}{s^2+\left[(1-D_y)\frac{R_c}{L}+\frac{1}{R_{\rm Ld}C}\right]s+\frac{(1-D_y)^2}{LC}}. \tag{33}$$

According to Fig. 8, the expression of the duty-cycle-to-output-voltage transfer function incorporating inductor current feedback, $G_{\rm vd\_dis\_trail\_bst\_com}(s)$, is expressed as follows (34) shown at the bottom of this page.

Moreover, the coefficient of the constant term in the numerator of (34) can be approximated as follows:

$$1+\frac{2R_c}{(1-D_y)R_{\rm Ld}}-\frac{(1-D_y)^2R_cT_s}{2L}\approx 1. \tag{35}$$

Thus, (34) can be approximated as follows:

Comparing (22) and (36) as shown at the bottom of this page, it can be found that $G_{\rm vd\_dis\_trail\_bst\_com}(s)$ and $G_{\rm vd\_dis\_lead\_bst}(s)$ are approximately the same under the condition that

$$R_c>>\frac{D_yT_s}{2C}(1-D_y). \tag{37}$$

Thus, the duty-cycle-to-output-voltage transfer function of the trailing-edge modulated boost converter with inductor current feedback is the same as that of the leading-edge modulation. Both the Bode diagrams of $G_{\rm vd\_dis\_trail\_bst\_com}(s)$ and $G_{\rm vd\_dis\_lead\_bst}(s)$ are shown in Fig. 9, verifying the close resemblance of the two transfer functions. Therefore, the characteristics of the leading-edge modulation can be equivalently obtained by incorporating inductor current feedback into the trailing-edge modulated converters.

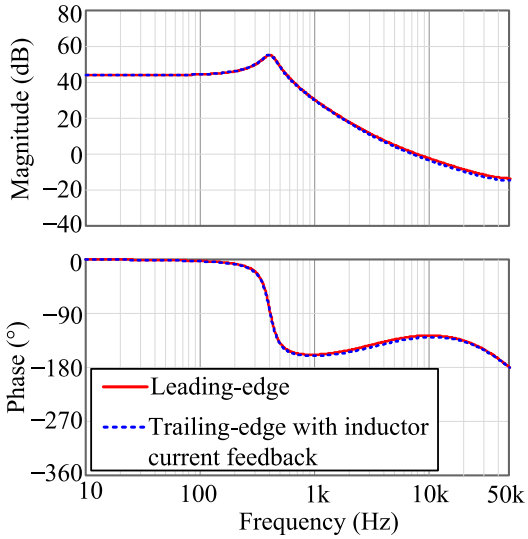

Fig. 9. Bode diagrams of $G_{\rm vd\_dis\_trail\_bst\_com}(s)$ and $G_{\rm vd\_dis\_lead\_bst}(s)$.

Fig. 10 shows the implementation circuit of the inductor current feedback control for the boost converter. The inductor current is sensed through resistor R_s, and then amplified R_c/R_s times via operational amplifier A1, giving i_LR_c. Then, i_LR_c is processed by a first-order high-pass filter to eliminate its dc component and then injected into the output voltage feedback component via operational amplifier A2, which is taken as the actual output voltage feedback component to be regulated by the compensator constructed by operational amplifier A3. It should be noted that the high-pass filter is necessary, and its corner frequency should be much lower than the switching frequency of the converter to avoid distortion of the inductor current.

V. Experimental Verification

In order to verify the accuracy of the theoretical analysis above, two prototypes (buck, boost converters) are fabricated and tested in the laboratory. The main circuit parameters are shown in Appendix B. The Bode diagrams of $G_{\rm vd\_dis}(s)$ under the leading-edge and trailing-edge modulation are plotted using the network analyzer Agilent E5061B, and the stability of the

$$G_{\rm vd\_dis\_trail\_bst\_com}(s)=R_cG_{\rm id\_dis\_trail\_bst}(s)+G_{\rm vd\_dis\_trail\_bst}(s)=\frac{V_{\rm in}}{LC}\frac{1+\frac{2R_c}{(1-D_y)R_{\rm Ld}}-\frac{(1-D_y)^2R_cT_s}{2L}+s\left[\frac{R_cC}{1-D_y}-\frac{D_yT_s}{2}-\frac{L}{(1-D_y)^2R_{\rm Ld}}\right]\left[1-\frac{sT_s}{2}+\left(\frac{sT_s}{\pi}\right)^2\right]-\left(\frac{sT_s}{\pi}\right)^2}{s^2+s\left[(1-D_y)\frac{R_c}{L}+\frac{1}{R_{\rm Ld}C}\right]+\frac{(1-D_y)^2}{LC}} \tag{34}$$

$$G_{\rm vd\_dis\_trail\_bst\_com}(s)=\frac{V_{\rm in}}{LC}\frac{1+s\left[\frac{R_cC}{1-D_y}-\frac{D_yT_s}{2}-\frac{L}{(1-D_y)^2R_{\rm Ld}}\right]\left[1-\frac{sT_s}{2}+\left(\frac{sT_s}{\pi}\right)^2\right]-\left(\frac{sT_s}{\pi}\right)^2}{s^2+s\left[(1-D_y)\frac{R_c}{L}+\frac{1}{R_{\rm Ld}C}\right]+\frac{(1-D_y)^2}{LC}} \tag{36}$$

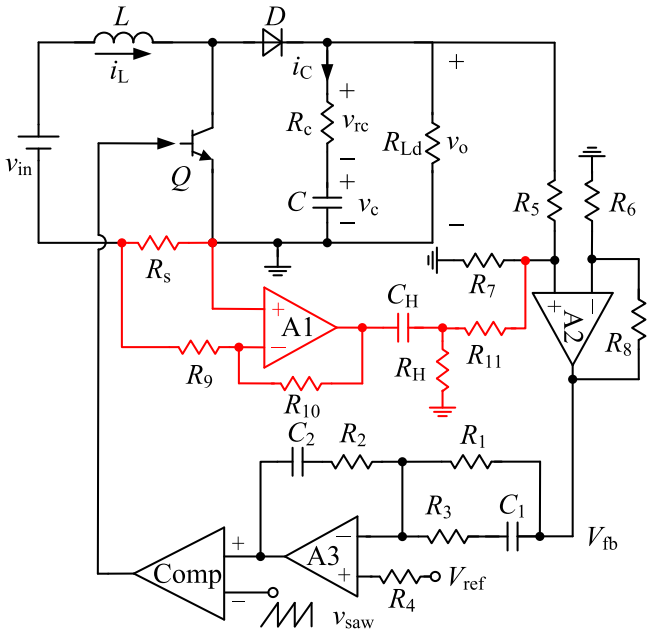

Fig. 10. Circuit schematic of introducing inductor current feedback into the trailing-edge modulated boost converter.

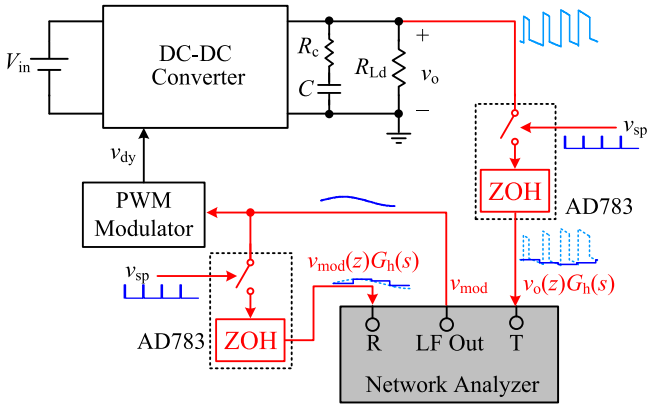

Fig. 11. Measurement circuit for the Bode diagrams of $G_{\text{vd\_dis}}(s)$.

converters is estimated for verification of the accuracy of the analysis.

A commonly used technique to measure G_{vd} is to inject a sinusoidal perturbation v_{mod} (with a dc bias to provide dc operating point) into the modulation signal to generate a perturbed duty cycle. Then, the modulation signal and the output voltage responses are directly sent to the network analyzer. However, as discussed in Section II, the output voltage and the modulation signal should be sampled at the intersecting instant before being sent to the network analyzer. The measurement principle is shown in Fig. 11, where v_{sp} is the sampling pulse. To lower the switching noise and simplify the implementation, a zero-order hold is introduced after the sampling switch. Since the sampling switch and the zero-order hold are available in control ICs, such as AD783, the implementation is very simple. The measured

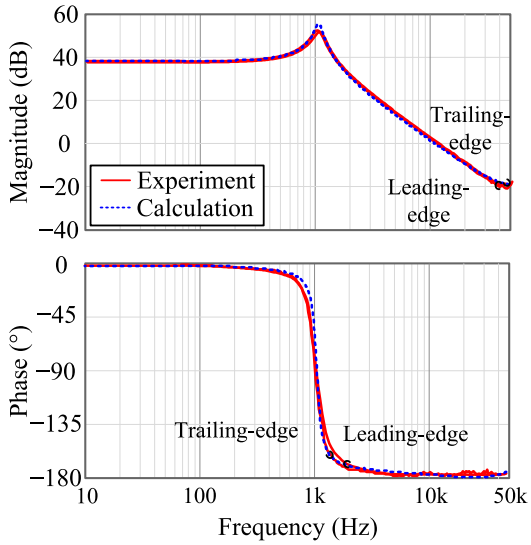

Fig. 12. Bode diagrams of calculated and measured $G_{\text{vd\_dis\_bu}}(s)$.

$G_{\text{vd\_dis}}(z)$ is

$$G_{\text{vd\_dis}}(z) = V_m \frac{v_o(z)G_h(s)}{v_{\text{mod}}(z)G_h(s)} = V_m \frac{v_o(z)}{v_{\text{mod}}(z)} \tag{38}$$

where V_m and $G_h(s)$ are the amplitude of the triangular carrier wave and the transfer function of ZOH, respectively. Also, $G_h(s)$ has no effect on the final result because it can be canceled from both the numerator and denominator.

A. Experimental Results of Buck Converter

Fig. 12 gives the Bode diagrams of $G_{\text{vd\_dis\_bu}}(s)$ by both the approximate model and measured results. As shown in the results, the leading-edge modulation and trailing-edge modulation show no difference, and the calculated and measured results are well matched, verifying the accuracy of the approximate discrete-time model.

The compensator for the buck converter is expressed as follows:

$$G_{\text{v\_bu}}(s) = \left(3.3 + \frac{19608.6}{s}\right) \frac{1 + \frac{s}{6447}}{1 + \frac{s}{116\,100}}. \tag{39}$$

The steady-state experimental waveforms under both leading-edge and trailing-edge modulations are shown in Fig. 13. Obviously, consistent with the theoretical analysis, the converter is stable under both PWM schemes.

B. Experimental Results of Boost Converter

Fig. 14 illustrates the Bode diagrams of $G_{\text{vd\_dis\_bst}}(s)$ by both the approximate model and measured results. Here, results of the leading-edge modulation and trailing-edge modulation coincide with the corresponding measured results, which verify the accuracy of the approximate discrete-time model. In addition, it can be observed that the trailing-edge modulation shows a lagging phase angle relative to the leading-edge modulation, which is consistent with the theoretical analysis.

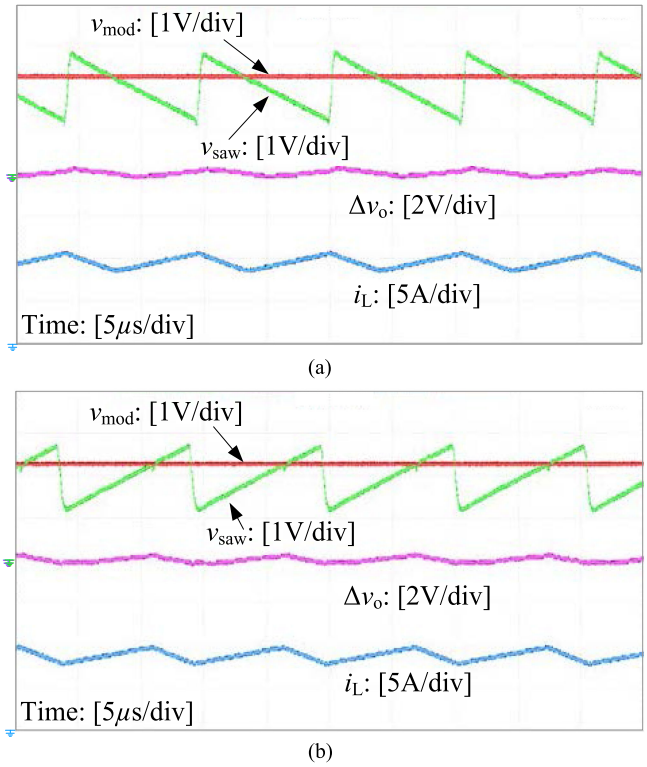

Fig. 13. Experimental waveforms of the buck converter under (a) leading-edge modulation and (b) trailing-edge modulation.

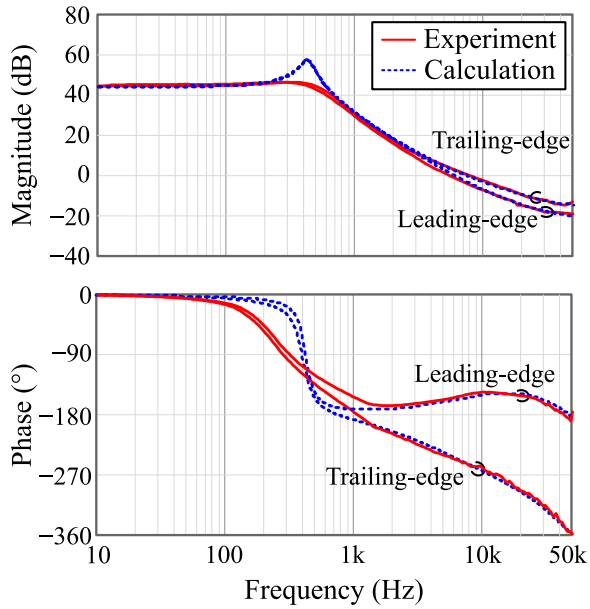

Fig. 14. Bode diagrams of calculated and measured $G_{vd\_dis\_bst}(s)$.

Generally, for a trailing-edge modulated boost converter, the achievable closed-loop bandwidth is one-fifth of that of the right-half-plane (RHP) zero under voltage-mode control [28]. In this paper, the RHP zero is located at 4 kHz, therefore the cut-off frequency is set at 800 Hz to guarantee sufficient stability margin of the boost converter under trailing-edge modulation. Considering this, the first compensator for the boost converter is designed as follows:

$$G_{v\_bst1}(s) = \left(0.37 + \frac{64.2}{s}\right)\frac{1+\frac{s}{4080}}{1+\frac{s}{23\,380}}. \tag{40}$$

In this case, when adopting the trailing-edge modulation, the cut-off frequency is $f_c = 800$ Hz and the phase margin is 35°, when adopting the leading-edge modulation, the cut-off frequency is $f_c = 800$ Hz and the phase margin is 50°. Thus, the converter should be stable under both modulations according to the proposed model. Experimental waveforms corresponding to the leading-edge modulation and the trailing-edge modulation are shown in Fig. 15(a) and (b), respectively. Here, the boost converter is stable under both modulations, which is in agreement with the theoretical analysis.

Since the RHP zero is eliminated under leading-edge modulation, the bandwidth of the boost converter under leading-edge modulation can be significantly increased. To verify this conclusion, the second compensator for the boost converter is designed to be

$$G_{v\_bst2}(s) = \left(1.1 + \frac{1099}{s}\right)\frac{1+\frac{s}{1023}}{1+\frac{s}{14\,706}}. \tag{41}$$

In this case, when adopting the trailing-edge modulation, the cut-off frequency is $f_c = 4.1$ kHz and the phase margin is $-20°$. Thus, the converter should be unstable. When adopting the leading-edge modulation, the cut-off frequency is $f_c = 3.9$ kHz and the phase margin is 45°. Thus, the converter should be stable. Experimental waveforms corresponding to the leading-edge modulation and the trailing-edge modulation are shown in Fig. 16(a) and (b), respectively. Here, the boost converter is stable under the leading-edge modulation, but becomes unstable under the trailing-edge modulation, and the unstable oscillation frequency is about 4.4 kHz, which is less than 1/20 of the switching frequency, thus can be regarded as a kind of slow-scale instability [29], [30]. The experimental results are well in agreement with the analysis.

According to the analysis discussed in Section IV, the trailing-edge modulated boost converter is stabilized by applying the modulation signal ZOH method or the inductor current feedback method. Fig. 17 gives the experimental waveforms of the trailing-edge modulated boost converter with $G_{v\_bst2}(s)$ as the compensator under the application of the modulation signal ZOH method. Fig. 17(a) shows the regulation of the duty cycle of the boost converter under this method. From Fig. 17(a), the sampling pulse v_{sp} is generated by the clock signal of the PWM controller UC3823DW, and is slightly leading the gate drive of the switch. At the falling edge of v_{sp}, the modulation signal is sampled and held, resulting in v_{mod_ZOH}. When v_{mod_ZOH} intersects the carrier wave, the switch turns OFF. In Fig. 17(b), the key experimental waveforms of the boost converter with the modulation signal ZOH method are given, where we can see that the boost converter is stabilized by the proposed method.

Fig. 18 provides the experimental waveforms when the inductor current feedback method is applied. It can be seen that the boost converter also becomes stable under this method.

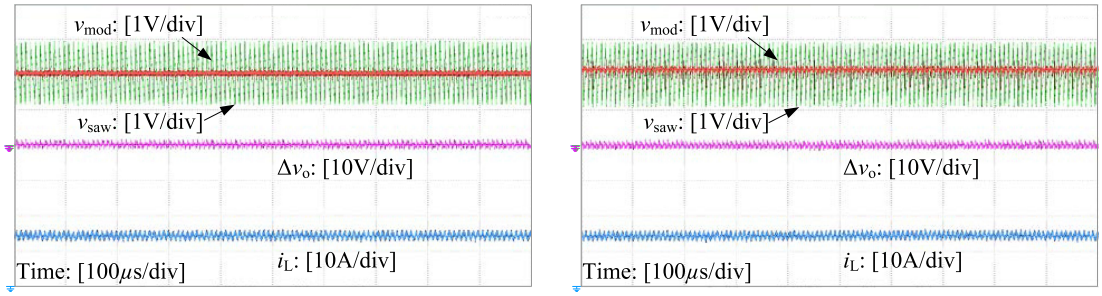

Fig. 15. Experimental waveforms of the boost converter with $G_{v\_bst1}(s)$ as the compensator under (a) leading-edge modulation and (b) trailing-edge modulation.

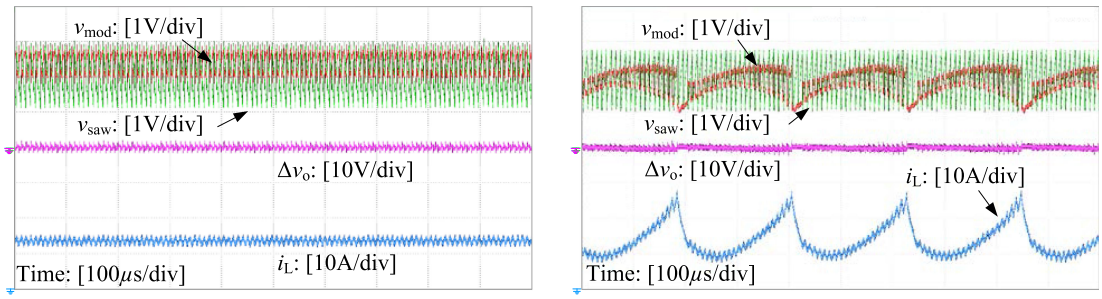

Fig. 16. Experimental waveforms of the boost converter with $G_{v\_bst2}(s)$ as the compensator under (a) leading-edge modulation and (b) trailing-edge modulation.

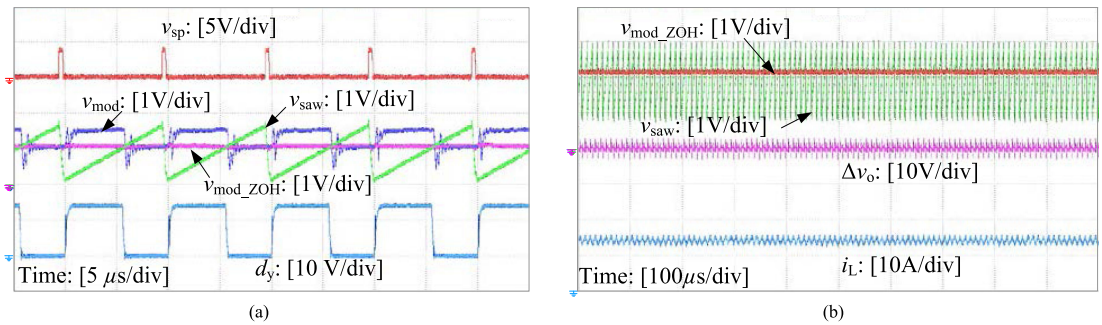

Fig. 17. Experimental waveforms of the trailing-edge modulated boost converter with modulation signal ZOH method. (a) Regulation process of the duty cycle. (b) Waveforms of the main circuit.

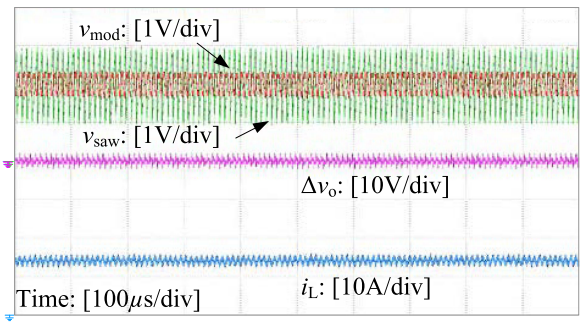

Fig. 18. Experimental waveforms of the trailing-edge modulated boost converter under the inductor current feedback scheme.

C. Transient Response Experimental Results of Boost Converter

Figs. 19–22 show the transient responses of the boost converter with trailing-edge modulation, leading-edge modulation, the modulation signal ZOH method, and the inductor current feedback method. Here, the compensator used in the trailing-edge modulation is $G_{v\_bst1}(s)$, while it is $G_{v\_bst2}(s)$ in the leading-edge modulation and the proposed control methods. The input voltage is stepped between 30 and 54 V, and the load is stepped between full load and 20% load. The overshoots/undershoots, and the settling time (2% of the final value) are tabulated in Table III. It can be found that as a consequence of the limited bandwidth, the trailing-edge modulation exhibits a relatively poor dynamic performance. In contrast, the dynamic performances of leading-edge modulation and proposed control methods are similar and are better than that of the trailing-edge modulation. To be specific, in response to a step change of the input voltage, the amount of overshoot or undershoot under the trailing-edge modulation is more than twice to that under the leading-edge modulation or the proposed control methods, and the settling time is three times longer. In response to a step change in the load, the overshoot

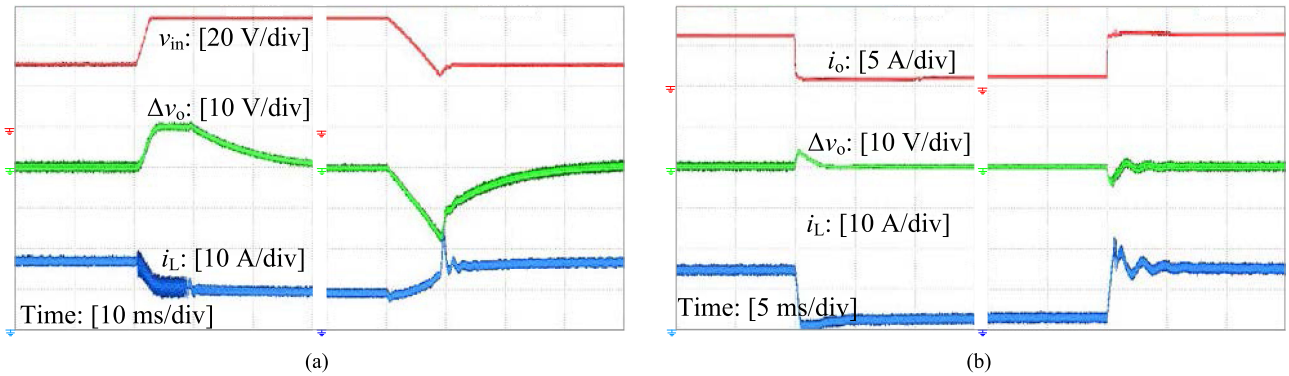

Fig. 19. Transient waveforms of the boost converter with trailing-edge modulation. (a) Input voltage steps between 30 and 54 V. (b) Load step between 20% load and full load.

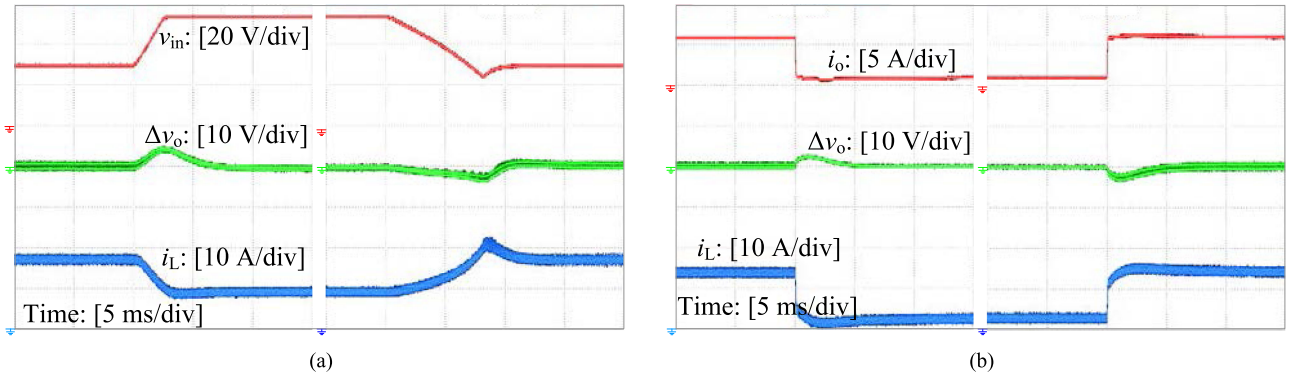

Fig. 20. Transient waveforms of the boost converter with leading-edge modulation. (a) Input voltage step between 30 and 54 V. (b) Load step between 20% load and full load.

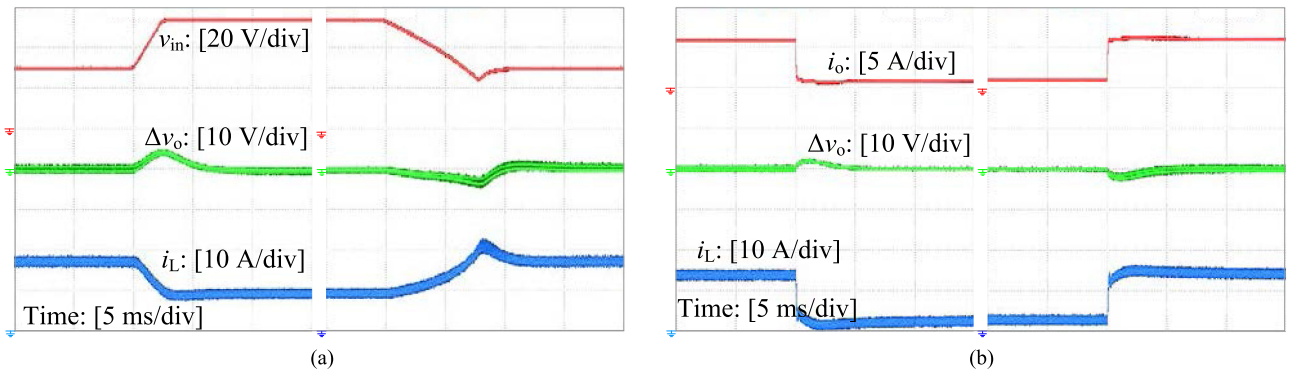

Fig. 21. Transient waveforms of the boost converter with modulation signal ZOH method. (a) Input voltage step between 30 and 60 V. (b) Load step between 20% load and full load.

or undershoot under the trailing-edge modulation is also higher than that under the leading-edge modulation or the proposed control methods. It should be noted that, from Table III, the settling times under the leading-edge modulation and the proposed methods during load step are slightly longer than those under the trailing-edge modulation using a standard 2% of the final value as the settling requirement. However, if assessed by the standard of 5% of the final value as the settling requirement, the settling times under the leading-edge modulation and the proposed methods during load step become zero since the overshoots/undershoots are all below 5%. As a conclusion, the leading-edge modulation and the proposed control methods have been shown to produce better dynamic performances.

From Fig. 22(b), it can be found that with the inductor current feedback method, the output voltage has an undershoot following the usual overshoot during a load step down, and has an overshoot following the usual undershoot during a load step

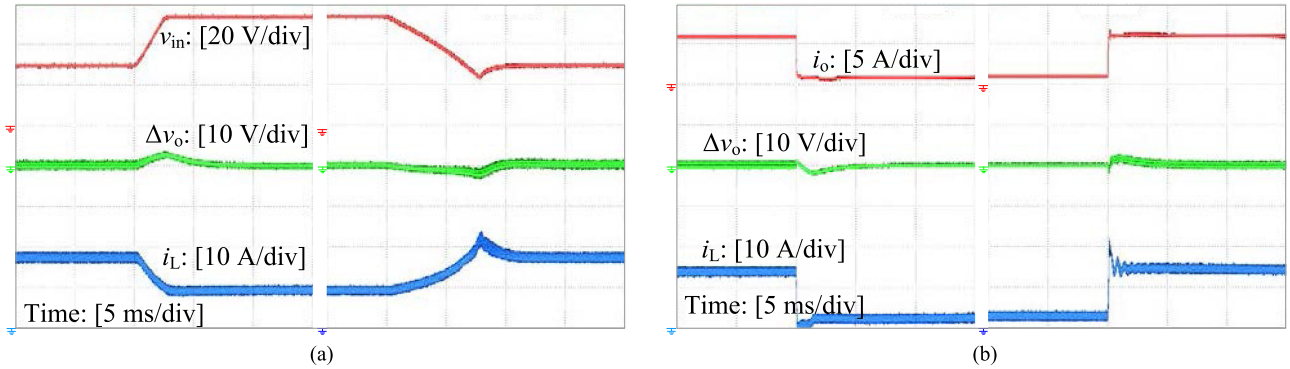

Fig. 22. Transient waveforms of the boost converter with inductor current feedback control method. (a) Input voltage step between 30 and 54 V. (b) Load step between 20% load and full load.

TABLE III
DYNAMIC PERFORMANCE INDICES OF THE BOOST CONVERTER UNDER DIFFERENT METHODS

Dynamic process	Dynamic peroformance	Trailing-edge	Leading-edge	ZOH method	Inductor current feedback
Load step up	Over/undershoot	5.9%	4.6%	3.7%	3.3%
	Settling time (ms)	3.4	4.2	3.7	3.6
Load step down	Over/undershoot	5.5%	3.5%	3.1%	3%
	Settling time (ms)	1.8	3.2	2.8	2.7
Input voltage step up	Over/undershoot	13.3%	6.25%	6%	4.1%
	Settling time (ms)	30	5.7	5.1	5.0
Input voltage step down	Over/undershoot	22.6%	5.1%	5.9%	3.9%
	Settling time (ms)	30.5	9.6	9.6	8.9

up. This can be explained as follows. When adding $kR_c i_L(t)$ into the output voltage, the feedback output voltage becomes $kv_c(t) + kR_c i_L(t)$ during the on-time, which is exactly the requirement for mimicking the leading-edge modulation, but it also becomes $kv_c(t) + 2kR_c i_L(t)$ during the off-time, which is not desirable. Obviously, there is an extra $kR_c i_L(t)$ during off time in the feedback output voltage compared with the leading-edge modulation. This extra $kR_c i_L(t)$ will lead to an extra modulation signal after being amplified by the compensator, which will affect the duty-cycle during transient processes. Fig. 23 gives the simulation waveforms during a step-up change of the load. From the top to bottom, the waveforms are the load current i_o, the triangle wave v_{saw}, the modulation signal v_{mod}, the extra modulation signal v_{mod_extra} produced by the extra $kR_c i_L(t)$, the ac component of the output voltage Δv_o, and the inductor current i_L. In Fig. 23, the value of v_{mod_extra} at the instant when the modulation signal intersects the triangle wave is highlighted with red dots. We can see that the extra modulation signal at the intersecting instant rises first after the load steps up, increasing the value of the real modulation signal v_{mod}. Therefore, the increase in the duty-cycle will be larger than in the case of the leading-edge modulation. As a consequence, the output voltage will have an overshoot following the usual undershoot during a step-up change of the load. Similarly, the output voltage will have an undershoot following the usual overshoot during a step-down change of the load.

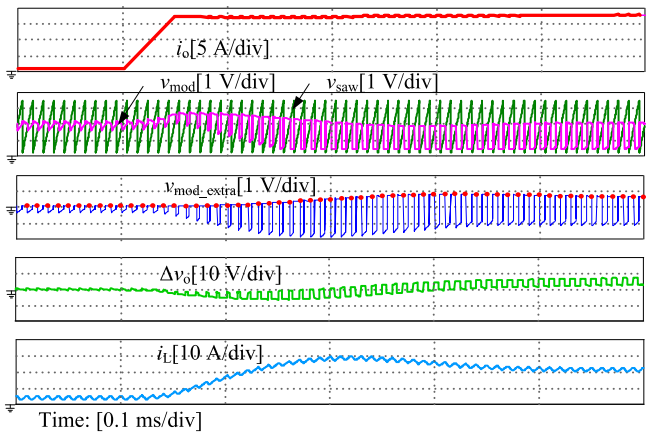

Fig. 23. Simulated load transient waveforms of the boost converter with inductor current feedback method during load step up.

VI. CONCLUSION

The discrete-time model with appropriate consideration of the sampling instant can well capture the behavior of dc–

dc converters under different types of PWM. To simplify the discrete-time model and provide useful physical insights, a unified method that converts the model from the discrete-time domain to the frequency domain applicable to all dc–dc converters is proposed. The resulting approximate model is much simpler compared with the accurate discrete-time model and can be accurate up to the Nyquist frequency. Using this approximate model, the stability of dc–dc converters using different modulation schemes is analyzed. The leading-edge modulated boost and buck–boost converters are shown to have better stability compared to the trailing-edge modulated converters. Since the trailing-edge modulation is more commonly used in practical applications, the modulation signal zero-order-hold method and the inductor current feedback method are proposed for the trailing-edge modulated boost and buck–boost converters mimicking the leading-edge modulated converters and hence achieving the same stability condition. Finally, experimental results verify the accuracy of the proposed model and the effectiveness of the proposed control methods.

APPENDIX A

This Appendix presents the proof of (8).

Define matrix $\mathbf{F}$ as

$$\mathbf{F} = s\mathbf{I} - \mathbf{A}_1 D_y - \mathbf{A}_2(1 - D_y). \tag{A1}$$

For typical dc–dc converters, matrix $\mathbf{F}$ is diagonalizable in the complex frequency domain [31]. As a result, there exists an invertible matrix $\mathbf{P}$ and a diagonal matrix $\mathbf{\Lambda}$ [32], satisfying

$$\mathbf{P}^{-1}\mathbf{F}\mathbf{P} = \mathbf{\Lambda}. \tag{A2}$$

According to the definition of matrix function [32], we have

$$e^{\mathbf{F}T_s} = \mathbf{I} + \mathbf{F}T_s + \frac{(\mathbf{F}T_s)^2}{2!} + \cdots + \frac{(\mathbf{F}T_s)^n}{n!} + \cdots. \tag{A3}$$

Then, we have

$$\mathbf{P}^{-1}e^{\mathbf{F}T_s}\mathbf{P} = \mathbf{P}^{-1}\left[\mathbf{I} + \mathbf{F}T_s + \frac{(\mathbf{F}T_s)^2}{2!} + \cdots + \frac{(\mathbf{F}T_s)^n}{n!} + \cdots\right]\mathbf{P}. \tag{A4}$$

According to (A2), (A4) can be rewritten as follows:

$$\mathbf{P}^{-1}e^{\mathbf{F}T_s}\mathbf{P} = \mathbf{I} + \mathbf{\Lambda}T_s + \frac{(\mathbf{\Lambda}T_s)^2}{2!} + \cdots + \frac{(\mathbf{\Lambda}T_s)^n}{n!} + \cdots. \tag{A5}$$

Since the state matrices of the three basic dc–dc converters studied in this paper are all second-order matrices, we can set the diagonal matrix $\mathbf{\Lambda}$ as follows:

$$\mathbf{\Lambda} = \begin{bmatrix} \Lambda_1 & 0 \\ 0 & \Lambda_2 \end{bmatrix} \tag{A6}$$

where Λ_1 and Λ_2 are not zero. Substituting (A6) into (A5) yields the following:

For the exponential function e^x, the Taylor series is represented as follows [33]:

$$e^x = 1 + x + \frac{x^2}{2!} + \cdots + \frac{x^n}{n!} + \cdots. \tag{A8}$$

Therefore, (A7) as shown at the bottom of this page, can be rewritten as follows:

$$\mathbf{P}^{-1}e^{\mathbf{F}T_s}\mathbf{P} = \begin{bmatrix} e^{\Lambda_1 T_s} & 0 \\ 0 & e^{\Lambda_2 T_s} \end{bmatrix} = \begin{bmatrix} \frac{e^{0.5\Lambda_1 T_s}}{e^{-0.5\Lambda_1 T_s}} & 0 \\ 0 & \frac{e^{0.5\Lambda_2 T_s}}{e^{-0.5\Lambda_2 T_s}} \end{bmatrix}. \tag{A9}$$

Using the second-order Padé approximants, for the frequency range lower than half the switching frequency f_s, we have the following approximate substitutions:

$$\frac{e^{0.5\Lambda_1 T_s}}{e^{-0.5\Lambda_1 T_s}} \approx \frac{1 + 0.5\Lambda_1 T_s + \left(\frac{\Lambda_1 T_s}{\pi}\right)^2}{1 - 0.5\Lambda_1 T_s + \left(\frac{\Lambda_1 T_s}{\pi}\right)^2} \tag{A10a}$$

$$\frac{e^{0.5\Lambda_2 T_s}}{e^{-0.5\Lambda_2 T_s}} \approx \frac{1 + 0.5\Lambda_2 T_s + \left(\frac{\Lambda_2 T_s}{\pi}\right)^2}{1 - 0.5\Lambda_2 T_s + \left(\frac{\Lambda_2 T_s}{\pi}\right)^2}. \tag{A10b}$$

Substituting (A10) into (A9) yields (A11). From (A11), $e^{\mathbf{F}Ts}$ can be deduced as (A12). Moreover, substitution of (A1) into (A12) leads to (A13), which is exactly the result given in (8)

$$\begin{aligned}\mathbf{P}^{-1}e^{\mathbf{F}T_s}\mathbf{P} &\approx \begin{bmatrix} \frac{1+0.5\Lambda_1 T_s+\left(\frac{\Lambda_1 T_s}{\pi}\right)^2}{1-0.5\Lambda_1 T_s+\left(\frac{\Lambda_1 T_s}{\pi}\right)^2} & 0 \\ 0 & \frac{1-0.5\Lambda_2 T_s+\left(\frac{\Lambda_2 T_s}{\pi}\right)^2}{1+0.5\Lambda_2 T_s+\left(\frac{\Lambda_2 T_s}{\pi}\right)^2} \end{bmatrix} \\ &= \begin{bmatrix} 1 + 0.5\Lambda_1 T_s + \left(\frac{\Lambda_1 T_s}{\pi}\right)^2 & 0 \\ 0 & 1 + 0.5\Lambda_2 T_s + \left(\frac{\Lambda_2 T_s}{\pi}\right)^2 \end{bmatrix} \\ &\quad \cdot \begin{bmatrix} 1 - 0.5\Lambda_1 T_s + \left(\frac{\Lambda_1 T_s}{\pi}\right)^2 & 0 \\ 0 & 1 - 0.5\Lambda_2 T_s + \left(\frac{\Lambda_2 T_s}{\pi}\right)^2 \end{bmatrix}^{-1} \\ &= \left[\mathbf{I} + 0.5\mathbf{\Lambda}T_s + \frac{1}{\pi^2}(\Lambda T_s)^2\right]\left[\mathbf{I} - 0.5\mathbf{\Lambda}T_s + \frac{1}{\pi^2}(\Lambda T_s)^2\right]^{-1}\end{aligned} \tag{A11}$$

$$\begin{aligned}e^{\mathbf{F}T_s} &= \left\{\mathbf{P}\left[\mathbf{I} + 0.5\mathbf{\Lambda}T_s + \frac{1}{\pi^2}(\mathbf{\Lambda}T_s)^2\right]\mathbf{P}^{-1}\right\} \\ &\quad \cdot \left\{\mathbf{P}\left[\mathbf{I} - 0.5\mathbf{\Lambda}T_s + \frac{1}{\pi^2}(\mathbf{\Lambda}T_s)^2\right]^{-1}\mathbf{P}^{-1}\right\} \\ &= \left[\mathbf{I} + 0.5\mathbf{F}T_s + \frac{1}{\pi^2}(\mathbf{F}T_s)^2\right]\left[\mathbf{I} - 0.5\mathbf{F}T_s + \frac{1}{\pi^2}(\mathbf{F}T_s)^2\right]^{-1}\end{aligned} \tag{A12}$$

$$\mathbf{P}^{-1}e^{\mathbf{F}T_s}\mathbf{P} = \begin{bmatrix} 1 + \Lambda_1 T_s + \frac{(\Lambda_1 T_s)^2}{2!} + \cdots + \frac{(\Lambda_1 T_s)^n}{n!} + \cdots & 0 \\ 0 & 1 + \Lambda_2 T_s + \frac{(\Lambda_2 T_s)^2}{2!} + \cdots + \frac{(\Lambda_2 T_s)^n}{n!} + \cdots \end{bmatrix} \tag{A7}$$

TABLE IV
PARAMETERS OF THE BUCK CONVERTER

Parameter	Symbol	Value	Parameter	Symbol	Value
Input votlage	V_{in}	80 V	Output capacitor	C	220 μF
Output voltage	V_{o}	54 V	Capacitor ESR	R_{c}	10 mΩ
Inductor	L	95 μH			

TABLE V
PARAMETERS OF THE BOOST CONVERTER

Parameter	Symbol	Value	Parameter	Symbol	Value
Input votlage	V_{in}	36 V	Output capacitor	C	300 μF
Output voltage	V_{o}	80 V	Capacitor ESR	R_{c}	0.07 Ω
Inductor	L	95 μH			

TABLE VI
PARAMETERS OF THE BUCK–BOOST CONVERTER

Parameter	Symbol	Value	Parameter	Symbol	Value
Input votlage	V_{in}	36 V	Output capacitor	C	470 μF
Output voltage	V_{o}	80 V	Capacitor ESR	R_{c}	68 mΩ
Inductor	L	60 μH			

$$e^{[s\mathbf{I}-\mathbf{A}_1 D_y-\mathbf{A}_2(1-D_y)]T_s} \approx \left\{\mathbf{I}+0.5\left[s\mathbf{I}-\mathbf{A}_1 D_y-\mathbf{A}_2\left(1-D_y\right)\right]T_s + \frac{\left[s\mathbf{I}-\mathbf{A}_1 D_y-\mathbf{A}_2\left(1-D_y\right)\right]^2 T_s^2}{\pi^2}\right\}\cdot \left\{\mathbf{I}-0.5\left[s\mathbf{I}-\mathbf{A}_1 D_y-\mathbf{A}_2\left(1-D_y\right)\right]T_s + \frac{\left[s\mathbf{I}-\mathbf{A}_1 D_y-\mathbf{A}_2\left(1-D_y\right)\right]^2 T_s^2}{\pi^2}\right\}^{-1}. \quad \text{(A13)}$$

APPENDIX B

In this paper, for the buck, boost, and buck–boost converters, the output power $P_{\text{o}} = 500$ W, the switching frequency $f_s = 100$ kHz, and the gain of the voltage sensor $H_v = 0.05$, the amplitude of triangle carrier wave $V_m = 1.75$ V. The other main circuit parameters of these three converters are given in Tables IV–VI.

REFERENCES

[1] G. W. Wester and R. D. Middlebrook, "Low-frequency characterization of switched dc-dc converters," *IEEE Trans. Aerosp. Electron. Syst.*, vol. AES-9, no. 3, pp. 376–385, May 1973.

[2] R. D. Middlebrook and S. Cuk, "A general unified approach to modeling switching converter power stages," in *Proc. IEEE Power Electron. Spec. Conf.*, 1976, pp. 18–34.

[3] V. Vorpérian, "Simplified analysis of PWM converter using model of PWM switch, Part 1: Continuous conduction mode," *IEEE Trans. Aerosp. Electron. Syst.*, vol. AES-26, no. 3, pp. 490–496, May 1990.

[4] V. Vorpérian, "Simplified analysis of PWM converter using model of PWM switch. Part 2: Discontinuous conduction mode," *IEEE Trans. Aerosp. Electron. Syst.*, vol. AES-26, no. 3, pp. 497–505, May 1990.

[5] P. R. K. Chetty, "Current injected equivalent circuit approach to modeling switching dc-dc converters," *IEEE Trans. Aerosp. Electron. Syst.*, vol. AES-17, no. 6, pp. 802–808, Nov. 1981.

[6] R. D. Middlebrook, "Small-signal modeling of pulse-width modulated switched-mode power converter," *Proc. IEEE*, vol. 76, no. 4, pp. 343–354, Apr. 1988.

[7] A. R. Brown and R. D. Middlebrook, "Sampled-data modeling of switching regulators," in *Proc. IEEE Power Electron. Spec. Conf.*, 1990, pp. 349–369.

[8] F. C. Lee, R. P. Iwens, Y. Yu, and J. E. Triner, "Generalized computer aided discrete time domain modeling and analysis of dc-dc converters," *IEEE Trans. Ind. Electron. Control Inst.*, vol. IECI-26, no. 2, pp. 58–69, May 1979.

[9] F. C. Lee and Y. Yu, "Modeling of switching regulator power stages with and without zero-inductor-current dwell time," *IEEE Trans. Ind. Electron. Control Inst.*, vol. IECI-26, no. 3, pp. 142–150, Aug. 1979.

[10] A. Capel, J. G. Ferrante, and R. Prajoux, "State variable stability analysis of multi-loop PWM controlled dc/dc regulators in light and heavy mode," in *Proc. IEEE Power Electron. Spec. Conf.*, 1975, pp. 91–103.

[11] D. Yang, X. Ruan, and H. Wu, "A real-time computation method with dual sampling modes to improve the current control performance of the LCL-type grid-connected inverter," *IEEE Trans. Ind. Electron.*, vol. 62, no. 7, pp. 4563–4572, Jul. 2015.

[12] D. Pan, X. Ruan, C. Bao, W. Li, and X. Wang, "Optimized controller design for LCL-type grid-connected inverter to achieve high robustness against grid-impedance variation," *IEEE Trans. Ind. Electron.*, vol. 62, no. 3, pp. 1537–1547, Mar. 2014.

[13] D. M. Van de Sype, K. D. Gusseme, A. P. M. Van den Bossche, and J .A. Melkebeek, "Small-signal Laplace-domain analysis of uniformly sampled pulse-width modulators," in *Proc. IEEE Power Electron. Spec. Conf.*, 2004, vol. 6, pp. 4292–4298.

[14] D. Maksimovic and R. Zane, "Small-signal discrete-time modeling of digitally controlled PWM converters," *IEEE Trans. Power Electron.*, vol. 22, no. 6, pp. 2552–2556, Nov. 2007.

[15] V. Yousefzadeh, M. Shirazi, and D. Maksimovic, "Minimum phase response in digitally controlled boost and flyback converters," in *Proc. IEEE Appl. Power Electron. Conf. Expo.*, Feb. 2007, pp. 865–870.

[16] S. Buso and P. Mattavelli, *Digital Control in Power Electronics*. Seattle, WA, USA: Morgan & Claypool, 2006.

[17] A. K. Singha and S. Kapat, "A unified framework for analysis and design of a digitally current-mode controlled buck converter, " *IEEE Trans. Cir. Syst. I*, vol. 63, no. 11, pp. 2098–2107, Nov. 2016.

[18] A. K. Singha and S. Kapat, "Analyzing the effects due to discontinuous output-voltage ripple in a digitally current-mode controlled boost converter, "*IET Power Electron.*, vol. 11, no. 6, pp. 1055–1065, May 2018.

[19] V. Rajasekaran, J. Sun, and B. S. Heck, "Bilinear discrete-time modeling for enhanced stability prediction and digital control design," *IEEE Trans. Power Electron.*, vol. 11, no. 6, pp. 381–389, Jan. 2003.

[20] D. Pan, X. Ruan, and X. Wang, "Direct realization of digital differentiators in discrete domain for active damping of LCL-Type grid-connected inverter," *IEEE Trans. Power Electron*, vol. 30, no. 10, pp. 8461–8473, Oct. 2018.

[21] A. G. Yepes, F. D. Freijedo, J. Doval-Gandoy, O. López, J. Malvar, and P. Fernandez-Comesana, "Effects of discretization methods on the performance of resonant controllers," *IEEE Trans. Power Electron.*, vol. 25, no. 7, pp. 1692–1712, Jul. 2010.

[22] G. C. Goodwin, S. F. Graebe, and M. E. Salgado, *Control System Design*. Upper Saddle River, NJ, USA: Prentice-Hall, 2000.

[23] D. J. Shortt and F. C. Lee, "Improved switching converter model using discrete and averaging techniques," *IEEE Trans. Aerosp. Electron. Syst.*, vol. AES-19, no. 2, pp. 190–202, Mar. 1983.

[24] D. J. Shortt and F. C. Lee, "Extensions of the discrete-average models for converter power stages," *IEEE Trans. Aerosp. Electron. Syst.*, vol. AES-20, no. 3, pp. 279–289, May 1984.

[25] D. M. Sable, B. H. Cho, and R. B. Ridley, "Use of leading-edge modulation to transform boost and flyback converters into minimum-phase-zero systems," *IEEE Trans. Power Electron.*, vol. 6, no. 4, pp. 704–711, Oct. 1991.

[26] X. Li, X. Ruan, Q. Jin, M. Sha, and C. K. Tse, "Approximate discrete-time modeling of dc-dc converters with consideration of the effects of pulse-width modulation," *IEEE Trans. Power Electron*, vol. 33, no. 8, pp. 7071–7082, Aug. 2018.

[27] A. V. Oppenheim and R. W. Schafer, *Discrete-Time Signal Processing*, 3rd ed. London, U.K.: Pearson Educ., 2009.
[28] S. W. Lee, "Practical feedback loop analysis for voltage-mode boost converter," Texas Instrum., Dallas, TX, USA, Appl. Rep. SLVA633, Jan. 2014, pp. 1–13.
[29] J. H. B. Deane and D. C. Hamill, "Instability, sub harmonics and chaos in power electronic systems," *IEEE Trans. Power Electron.*, vol. 5, no. 3, pp. 260–268, Jul. 1990.
[30] C. K. Tse and M. D. Bernardo, "Complex behavior in switching power converters," *Proc. IEEE*, vol. 90, no. 5, pp. 768–781, May 2002.
[31] G. Verghese, B. Levy, and T. Kailath, "A generalized state-space for singular systems," *IEEE Trans. Automat. Control*, vol. AC-26, no. 4, pp. 811–831, Aug. 1981.
[32] R. A. Horn and C. R. Johnson, *Matrix Analysis*, 2nd ed. London, U.K.: Cambridge Univ. Press, 2012.
[33] R. Walter, *Principles of Mathematical Analysis*, 3rd ed. New York, NY, USA: McGraw-Hill, 1976.

Xin Li received the B.S. degree in electrical engineering and automation from the Nanjing University of Aeronautics and Astronautics, Nanjing, China, where he is currently working toward the Ph.D. degree in electrical engineering, in 2012.

His current research interests include modeling and control of dc–dc converters and cascaded power systems.

Xinbo Ruan (M'97–SM'02–F'16) received the B.S. and Ph.D. degrees in electrical engineering from the Nanjing University of Aeronautics and Astronautics (NUAA), Nanjing, China, in 1991 and 1996, respectively.

In 1996, he joined the Faculty of Electrical Engineering Teaching and Research Division, NUAA, where he became a Professor with the College of Automation Engineering in 2002 and has been engaged in teaching and research in the field of power electronics. From August to October 2007, he was a Research Fellow with the Department of Electronic and Information Engineering, Hong Kong Polytechnic University, Hong Kong, China. Since March 2008, he has been also with the School of Electrical and Electronic Engineering, Huazhong University of Science and Technology, China. He is a Guest Professor with Beijing Jiaotong University, Beijing, China, Hefei University of Technology, Hefei, China, and Wuhan University, Wuhan, China. He has authored or coauthored 9 books and more than 200 technical papers published in journals and conferences. His main research interests include soft-switching dc–dc converters, soft-switching inverters, power factor correction converters, modeling the converters, power electronics system integration, and renewable energy generation systems.

Dr. Ruan is the recipient of the Delta Scholarship by the Delta Environment and Education Fund in 2003 and the Special Appointed Professor of the Chang Jiang Scholars Program by the Ministry of Education, China, in 2007. From 2005 to 2013, he served as the Vice President of the China Power Supply Society, and since 2008, he has been a member of the Technical Committee on Renewable Energy Systems within the IEEE Industrial Electronics Society. Currently, he serves as an Associate Editor for the IEEE TRANSACTIONS ON INDUSTRIAL ELECTRONICS, the IEEE TRANSACTIONS ON POWER ELECTRONICS, the IEEE JOURNAL OF EMERGING AND SELECTED TOPICS ON POWER ELECTRONICS, and the IEEE TRANSACTIONS ON CIRCUITS AND SYSTEMS-II.

Xiaoling Xiong received the B.Eng., M.Eng., and Ph.D degrees from the Nanjing University of Aeronautics and Astronautics, Nanjing, China, in 2007, 2010, and 2015, respectively.

She has spent a short of time with the Lighting Department, GE (China) Research & Development Center Co., Ltd, as an intern in 2010, and worked as a Research Assistant with the Department of Electronic and Information Engineering, Hong Kong Polytechnic University, from February 2011 to July 2012. She is currently a Lecturer with North China Electric Power University, Beijing, China. Her main research interests include HVDC system, modeling, analysis, and design power electronic systems and study the complex behavior in power electronic circuits.

Mengke Sha received the B.S. and M.S. degrees in electrical engineering from the Nanjing University of Aeronautics and Astronautics, Nanjing, China, in 2015, and 2018, respectively.

His main research interests include modeling and control of dc–dc converters.

Chi K. Tse (M'90–SM'97–F'06) received the B.Eng. (Hons.) degree in electrical engineering and the Ph.D. degree from the University of Melbourne, Australia, in 1987 and 1991, respectively.

He is currently a Chair Professor with the Hong Kong Polytechnic University, Hong Kong, China, with which he served as the Head of the Department of Electronic and Information Engineering from 2005 to 2012.

Dr. Tse was the recipient of a number of research and industry awards, including Prize Paper Awards by IEEE TRANSACTIONS ON POWER ELECTRONICS in 2001 and 2015, RISP Journal of Signal Processing Best Paper Award in 2014, the Best paper Award by International Journal of Circuit Theory and Applications in 2003, two Gold Medals at the International Inventions Exhibition in Geneva in 2009 and 2013, a Silver Medal at the International Invention Innovation Competition in Canada in 2016, and a number of recognitions by the academic and research communities, including honorary professorship by several Chinese and Australian universities, Chang Jiang Scholar Chair Professorship, IEEE Distinguished Lectureship, Distinguished Research Fellowship by the University of Calgary, Gledden Fellowship and International Distinguished Professorship-at-Large by the University of Western Australia. While with the Hong Kong Polytechnic University, he received the President's Award for Outstanding Research Performance twice, Faculty Research Grant Achievement Award twice, Faculty Best Researcher Award, and several teaching awards. He serves and has served as the Editor-in-Chief for the IEEE TRANSACTIONS ON CIRCUITS AND SYSTEMS II (2016–2019), IEEE CIRCUITS AND SYSTEMS MAGAZINE (2012–2015), the Editor-in-Chief of IEEE CIRCUITS AND SYSTEMS SOCIETY NEWSLETTER (since 2007), an Associate Editor for three IEEE Journal/Transactions, an Editor for *International Journal of Circuit Theory and Applications*, and is on the editorial boards of a few other journals. He also serves as a member of several government committees and panels.